Title

Quantitative Aspects of Image Intensifier- Television-Based Digital X-Ray Imaging

ISBN

9780306421884

Authors

Nalcioglu, O

Roeck, WW

Seibert, JA

et al.

Publication Date

1986

DOI

10.1007/978-1-4684-5068-2_5

5

Quantitative Aspects of Image Intensifier–Television-Based Digital X-Ray Imaging

O. Nalcioglu, W. W. Roeck, J. A. Seibert, A. V. Lando, J. M. Tobis, and W. L. Henry

1. INTRODUCTION

The utilization of video systems in diagnostic X-ray imaging has been around for quite some time. In addition to the visual diagnostic value of images obtained by such systems, the X-ray video systems also offer the potential for extracting quantitative information from the images. In this chapter we will not deal with quantitative determinations based on distance measurements. Even though the quantitation potential has been under investigation for the past decade,[1–3] it was not until the introduction of digital subtraction angiography (DSA)[4] that it received a concentrated effort. DSA makes it possible to visualize a small amount of radiopaque contrast agent within the vessels by means of various digital image enhancement methods which are discussed elsewhere in this book (Chapters 3, 7). Image processing takes place after the digitization of the video signal. Many users may assume that since the output is digital format, it must

O. Nalcioglu, W. W. Roeck, and A. V. Lando • Department of Radiological Sciences, University of California, Irvine, California 92716. Present address for A.V.L.: Philips Medical Systems, Inc., Shelton, Connecticut 06484. ***J. A. Seibert*** • Department of Radiology, University of California, Davis, California 95817. ***J. M. Tobis and W. L. Henry*** • Department of Medicine (Cardiology), University of California, Irvine, California 92716.

J. G. Kereiakes et al. (eds.), *Digital Radiography*

be as accurate as the data in computed tomography (CT) systems. Unfortunately, this is not true, and the reason is the existence of some basic differences between the CT and image intensifier–television (IT–TV)-based digital X-ray imaging systems. In digital fluoroscopy (or radiography), one usually uses large-area detectors such as an X-ray II. Due to poor detection geometry, the scattered photons within the patient seriously degrade the information obtained by a digital fluoroscopic system. In addition to poor geometry, the II detector itself is the source of another problem. This is the lateral propagation of light within the II, which is known as the veiling glare.[5] Veiling glare causes nonlinear upward shift of the video levels in the dark parts of an image. A final major problem is the beam hardening within the patient. The source of this problem is the preferential absorption of low-energy X-rays by an object, and the variation of effective beam energy as a function of object thickness. All these problems result in an overestimation of measured digital fluoroscopic numbers, but an underestimation of quantities which are based on the X-ray projection. Even though the three physical problems mentioned above reduce the accuracy of absolute measurements considerably, we have found in certain relative measurements that one may have a cancellation of errors.[6] However, the success in the computation of these parameters should not give a false sense of confidence. The development of correction techniques to reduce these errors is possible and some of them will be discussed in this chapter. Our basic philosophy differs substantially from many researchers who have attacked the same problems. We are not interested in applying empirical "Band-Aid" correction techniques which may only be applicable in a limited situation. We will discuss general methods which are applicable to broader phenomena, and, specifically, will improve the accuracy of digital fluoroscopic numbers for absolute measurements.

In Section 2, we will review the imaging system and various components. Section 3 will cover a detailed discussion of the characterization of the three physical problems mentioned earlier. Effect of physical degradation factors on the measurement of volumes is reviewed in Section 4. Techniques to reduce the effects of these problems will be presented in Section 5. Some examples of typical applications will be discussed in Section 6. A summary will be given in Section 7.

2. SYSTEM DESCRIPTION

Most of the imaging systems used in digital fluoroscopy utilize an II–TV camera as the receptor. A typical X-ray video system used in

diagnostic imaging is shown in Figure 1. The various components of the imaging chain are the X-ray generator, X-ray tube, II, TV camera, video processor, viewing and recording devices. In this chapter, we will discuss the propagation of a signal through the system and relevant equations describing this process. We will not be concerned with recording or viewing equipment.

2.1. X-Ray Generator and Tube

The term *generator* applies to that part of the system which controls and provides the high voltage and electrical power required to energize the X-ray tube. In quantitative measurements using an X-ray video system, it is essential that the X-ray tube output remains constant throughout the whole study. Pulse-to-pulse fluctuations in the X-ray fluence can be minimized by the use of 3-phase 12-pulse X-ray generators. For such generators, the maximum fluctuation in the tube output is about 3.5% of the peak voltage.

The X-ray tube should have a heat storage capacity of 300,000 heat units or more, so that a large flux of X-rays can be sent through the object. Another important aspect of the X-ray tube is the size and intensity distribution of the focal spot. The smaller the size, the smaller the objects we can image. Unfortunately, small focal spot size also implies loading a large amount of heat into a smaller area of anode, thus causing further X-ray flux limitations. For most applications, a 0.3/1.3-mm switchable focal spot is sufficient.

The function which describes the incident X-ray fluence at a location (x',y') in front of the object is given by

$$\text{Incident fluence} = N_0(x',y':E) \tag{1}$$

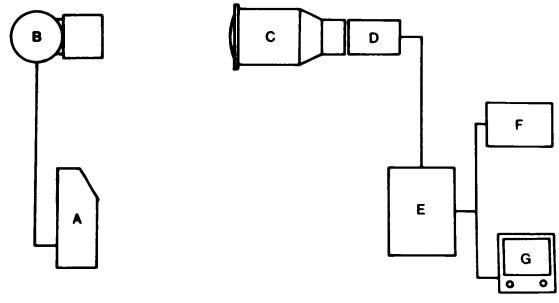

Figure 1. Overall imaging system: (A) X-ray generator, (B) X-ray tube, (C) image intensifier, (D) TV camera, (E) video image processor, (F) recording devices, and (G) monitor.

In writing Eq. (1), we assumed a parallel X-ray beam geometry and hence no dependence on z' where z' is the distance measured from the source. The energy variable E in Eq. (1) indicates the polychromatic nature of X-rays used explicitly.

2.2. Object

Let us assume that a three-dimensional object with a linear attenuation coefficient distribution $\mu(x,y,z:E)$ is placed into the X-ray beam. If the X-rays are emitted from the source in the z' direction, then the transmitted X-ray fluence is given by

$$N(x',y':E) = P(x',y':E) + S(x',y':E) \tag{2}$$

where S and P are the scatter and primary components, respectively. The primary X-ray distribution is related to the incident one by the following equation:

$$P(x',y':E) = N_0(x',y':E) \exp\left[-\int \mu(x',y',z':E)dz'\right] \tag{3}$$

where N_0 is the incident flux at location (x',y') and μ is the distribution of energy-dependent linear attenuation coefficients along the X-ray beam which is assumed to be parallel to the z' axis. The scatter component is related to the incident flux by a complex relationship. It is a complicated function of many variables including X-ray beam energy, object composition, and imaging geometry. A more detailed discussion of the scatter component will be presented in a later section.

2.3. Image Intensifier

All of the elements of an II tube are enclosed within a glass bottle that is highly evacuated. The input end of the tube has a coating consisting of the input phosphor, a thin transparent membrane, and the photocathode. The input phosphor is usually made of cesium iodide which absorbs the incident X-ray beam and emits visible light. Most IIs in use today have a cesium iodide input phosphor with a thickness of 100 mg/cm^2. The input phosphor thickness determines the detection efficiency as well as the spatial resolution capabilities of the II. The phosphor thickness is chosen as a trade-off between detection efficiency and spatial resolution. The limiting spatial resolution of a typical 9-inch II is about 4 lp/mm at the input phosphor. The detection efficiency is highly energy dependent. The visible light emitted from the phosphor passes through the thin mem-

brane and is absorbed in the photocathode. As a result of photoelectric absorption in the cathode, electrons are released to the interior of the II tube. These electrons are accelerated and focused toward the output phosphor which is much smaller in size than the input one. The output phosphor absorbs the kinetic energy of the electrons and produces an intensified visible light. A fraction of electrons and produced light photons scatter within the II, thus causing a degradation of image quality known as veiling glare. In regions of low transmission adjacent to regions of high transmission of the detected X-rays, electrons and light produced from the brighter areas spread into the darker areas. This nonuniform added bias affects the contrast response as well as the quantitative integrity of the information contained in the two-dimensional projection image. In addition to veiling glare, there might be spatial distortions due to poor electron optics.

The generation of light images by an II may be described by the following general equation:

$$I(x,y) = \alpha \iint D(x',y':E)T(x',y:x',y')N(x',y':E)dx'dy'dE \qquad (4)$$

where α is a constant of proportionality and $D(x',y':E)$ is the detection efficiency of the II at point (x',y') for an X-ray of energy E. The function $N(x',y':E)$, which was defined in Eq. (2), indicates the transmitted X-ray fluence of energy E at a location (x',y'). The transfer function T takes an X-ray absorption event from a location (x',y') on the input phosphor and generates light at location (x,y) at the output phosphor. In defining T, we assumed that it is independent of energy E, but the energy dependence could also be included in a straightforward manner. Equation (4) was originally proposed by Kruger.[7] The transfer function T includes the various image degradation processes such as veiling glare and spatial distortions.

2.4. Television Camera

The TV camera converts the light flux incident on its target surface into an electronic signal which will eventually be digitized. Most of the TV cameras used in digital fluoroscopy utilize a lead oxide (plumbicon) target. It is absolutely necessary to measure and know the response of the TV camera for quantitative applications. In a later section, we will discuss how this is done. The conversion of the light image $I(x,y)$ into a video image by the camera is described by

$$V(x,y) = f[I(x,y)] \qquad (5)$$

where I is defined in Eq. (4) and $f[I]$ is the transfer function for the process. In Eq. (5), $V(x,y)$ is the amplitude of the video signal at a location (x,y) within the image. Even though a general response function f is given in Eq. (5), in most cases it can be approximated by

$$f[I] = aI^{\gamma} \tag{6}$$

where a is a scaling factor and γ is a constant. For a plumbicon camera $\gamma \approx 1.0$.

2.5. Analog-to-Digital Converter

The analog-to-digital converter (ADC) is the device which converts the analog video signal into digital numbers. Due to the finite number of levels used, the ADC always adds additional noise (quantizing noise) to the signal. If the analog noise is normally distributed with a standard deviation σ, then an equation which relates the rms noise before and after the digitization can be derived. This relation is given by

$$\sigma_D/\sigma = 0.5\left[\sum_{i=0}^{\infty}(2i+1)^2 g_i(\epsilon/\sigma)\right]^{1/2}\epsilon/\sigma \tag{7}$$

where σ_D and σ are the rms noise after and before digitization and ϵ is the step size. The function $g_i(x)$ is defined by

$$g_i(x) = \text{erf}[0.5(i+1)x] - \text{erf}[0.5ix] \tag{8}$$

where erf is the error function.[8] The step size ϵ may also be expressed by

$$\epsilon = S/2^N \tag{9}$$

where S is the maximum linear video signal and N is the number of bits in the ADC. Using the definition for the signal-to-noise ratio (SNR)

$$\text{SNR} \equiv S/\sigma \tag{10}$$

one can relate ϵ/σ to SNR by

$$\epsilon/\sigma = \text{SNR}/2^N \tag{11}$$

The ratio σ_D/σ may be computed using Eq. (7) with $\epsilon/\sigma = 1$, 2, and 3. These results are given in Table 1.

TABLE 1. Variation of Digitized rms Noise (σ_D) as a Function of Step Size (ϵ)

ϵ/σ	1	2	3
σ_D/σ	1.03	1.17	1.50

It is seen that if ϵ is equal to the analog rms noise σ, digitization introduces only an additional 3% noise. One can also use Eq. (11) to compute the number of bits required for a given SNR. This is given by

$$N = \text{INT}\,[\ln(\text{SNR}/m)/\ln 2] + 1 \tag{12}$$

where $m = \epsilon/\sigma$ and INT [·] indicates integer truncation operation. Figure 2 shows the relation between the SNR and the number of bits required.

For an SNR of 500:1, one needs an 8-bit ADC for $\sigma_D/\sigma = 1.5$ (50% error) and a 9-bit ADC for a 3% error. For many dynamic clinical applications, the ADC should also be fast enough to digitize the images in real

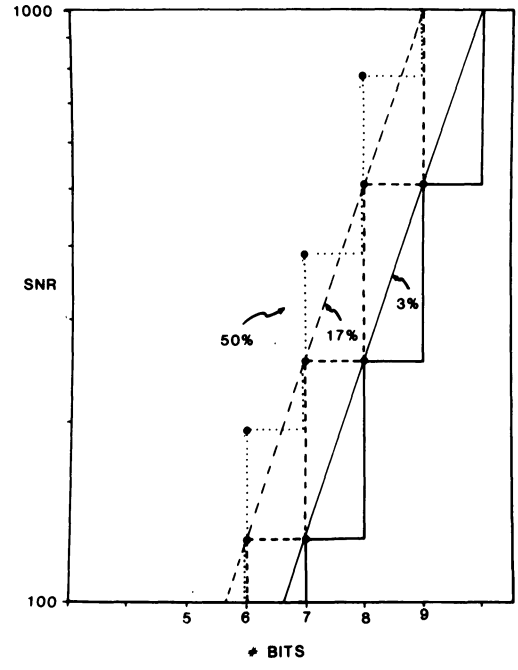

Figure 2. ln SNR versus number of bits.

time, i.e., 30 images/sec, with enough spatial resolution. A typical digitization format for real-time applications is 512 × 512 with 8 bits/pixel.

2.6. Image Acquisition Memory

After the data are digitized by the ADC, they are usually stored in a solid-state random access acquisition memory (RAM). For most radiologic applications, a matrix size of 512 × 512 pixels for the memory is sufficient. The size of the image matrix must be compatible with the TV camera resolution. Furthermore, each pixel must have at least as many bits as the number of bits of the ADC.

Larger memories are useful for image integration which is necessary in some applications. Even though acquisition memories as large as 2048 × 2048 pixels are also available, they do not seem to offer any additional advantage for quantitative applications.

2.7. Measurement of System Response

Here we will discuss the measurement of the TV camera and TV–II combination separately.

2.7.1. TV Camera Response

The purpose of this measurement is to determine the functional relationship given in Eq. (5) which relates the video signal V to the incident light level I. The TV camera response is measured by mounting the camera on an optical bench and varying the input light level incident on the camera.

The video voltage for each input light level I is measured to determine the response. The experimental results are given in Figure 3 for a 1-inch Syracuse Scientific plumbicon camera. In Figure 3 the video voltage versus the relative light input is plotted on a log–log graph. The response function for this camera was given by the simpler form shown in Eq. (6). If one substitutes Eq. (6) into Eq. (5) and takes the logarithm, one obtains

$$\ln V = \gamma \ln I + \ln a \tag{13}$$

The solid line in Figure 3 was obtained by a linear least-squares fit to the experimentally measured data (last point where camera saturation starts was not included). The fit had a correlation coefficient $r = 0.999$ and slope (γ) equal to 0.99. The maximum linear video signal from the camera was equal to 1 volt. The measured rms noise of the camera was determined

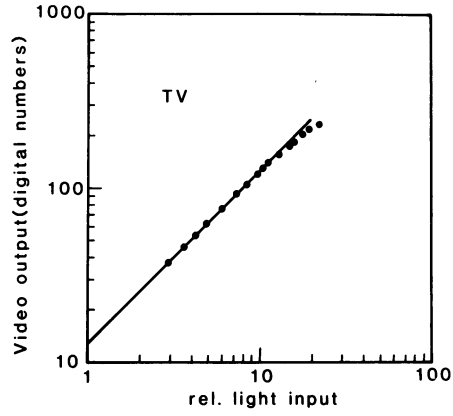

Figure 3. TV response as a function of relative light input.

to be 2 mV. Thus, the Syracuse Scientific camera used in our laboratory had a dynamic range of 500:1.

2.7.2. II–TV Response

Once the linear operating range of the TV camera is known, then the response of the II–TV system needs to be determined as a function of input X-ray exposure rate. This was done by varying the incident X-ray exposure rate by changing the X-ray mA while keeping the kVp constant. In this case, the video images were digitized and the II–TV response was determined from these measurements. The video voltage V is related to the input exposure rate X by

$$V = aX^{\gamma} \tag{14}$$

Taking the logarithm of both sides yields

$$\ln V = \gamma \ln X + \ln a \tag{15}$$

The experimental results for a Philips II–TV system are shown in Figure 4. The maximum linear voltage from the Philips camera was 920 mV and the rms noise was 4 mV. The Philips plumbicon camera had an SNR of 230:1. The straight line in Figure 4 is the II–TV response. The linear least-squares fit of Eq. (15) had a correlation coefficient $r = 0.99$ and $\gamma = 1.0$. Once the linear operation range of the TV camera and II–TV camera chain is known, one has to make sure to operate the system within this range so that there is a linear relationship between the output video

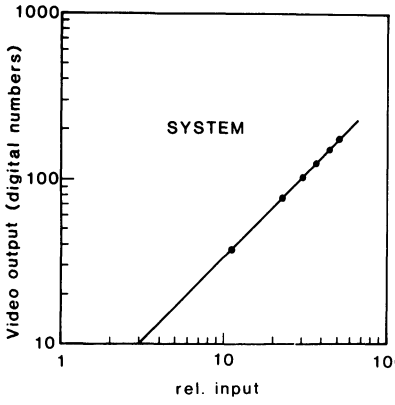

Figure 4. System response as a function of relative X-ray exposure.

voltage and the input X-ray exposure rate. Even if the response is not linear, one may still be able to linearize it by measuring the system response and using a lookup table.

2.8. System Spatial Resolution

Here we will closely follow the discussion given in Kruger *et al.*[9] If the focal spot of the X-ray tube has dimension b (mm), then the resolution limit (i.e., cutoff frequency) due to focal spot blurring is given by $f_{FS} = m/[b(m-1)]$ lp/mm as measured in the object plane for an object magnification m. For a 525-line TV camera, the vertical resolution is approximately 340 lines (see Hendee[10]). If we assume the same vertical and horizontal resolution for the TV camera, then the limiting spatial frequency is given by $f_c = 340/2D$ where D is the object size covering the full image field. In the object plane, this limiting resolution is given by $f_c = 340m/2D$. Finally, the limiting resolution in the object plane due to image digitization for a 512 × 512 image matrix is given by $f_D = 512m/2D$. In Figure 5, these three limiting frequencies are plotted as a function of magnification. It is seen that for $1 \leq m \leq 2$ (which is a reasonable range for most clinical applications), the bottleneck of spatial resolution is the 525-line TV camera. In this example, we assumed a 1.2-mm focal spot and a 9-inch II.

3. CHARACTERIZATION OF PHYSICAL DEGRADATION FACTORS

In this section we will present results which demonstrate effects of physical degradation factors on digital numbers measured with digital

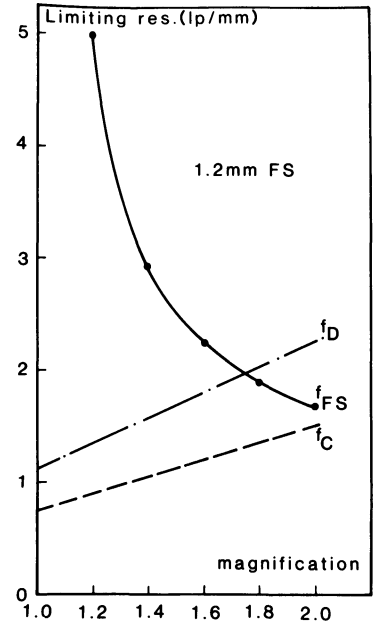

Figure 5. Resolution limits as a function of magnification. Solid curve, focal spot (1.2 mm); dashed curve, camera; dotted curve, digitizer cutoff frequencies for a 9-inch II.

fluoroscopic systems. The physical factors which will be considered are: beam hardening, X-ray scatter, and veiling glare. At this point, we will define a new function called the X-ray projection by

$$\Pr(L) = \ln[V(L = 0)/V(L)] \tag{16}$$

where $V(L)$ is the video signal (Eq. 5) at a location (x,y) for an object thickness of L. If the object is a composite material, then L is the upper limit of the integral in Eq. (3). For simplicity, we suppressed the dependence on (x,y) in Eq. (16) but it should be remembered that Pr is also a function of (x,y).

3.1. Beam Hardening

In order to study the effects of beam hardening alone, we have restricted the experimental setup to a narrow beam geometry, i.e., both the entrance and exit beams were collimated. Figure 6 illustrates the experimental setup. As a result of narrow beam geometry, we were able to eliminate scattered radiation within the object. The reduction of veiling glare[11–13] was accomplished by limiting the exposed field of view of the II to a small area (1 cm ∅). The reduction of the primary signal due to

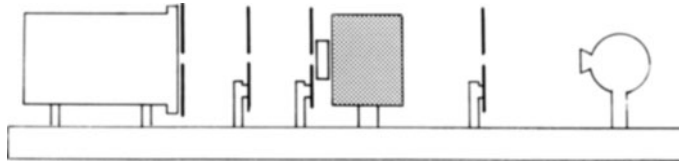

Figure 6. Narrow beam geometry on optical bench.

the limited II field of view was approximately 23% for the system used in these experiments. The reduction is due to the fact that light from the center escapes toward the edges, but since the remainder of the II was covered with lead, no light travels from the periphery to the center to compensate for the loss of light from the center to the periphery.

With this setup, Eqs. (2)–(6) can be combined to yield

$$V_1(x,y) = \beta \int D(x,y:E)P(x,y:E)dE \tag{17}$$

where the transfer function was taken to be $T(x,y;x',y') = \delta(x - x')\delta(y - y')$ and $\beta = a\alpha$. An experimental investigation of Eq. (17) was done by using various thicknesses of lucite as a scatter phantom, along with changes in X-ray tube filtration and iodine thickness in the X-ray beam. The imaging chain consisted of a Philips dual-mode (9 inch/5 inch) II, Model 9807 201 02 701. The X-ray tube was a Dunlee DU-175 0.3/1.0 dual-mode focal spot type. The X-ray generator was a 3-phase, 12-pulse system manufactured by Picker. The TV camera was a 1-inch Philips plumbicon system. Video images were digitized and stored in the memory of an American Edwards Laboratories Cardiac 1000 video image processor. The images were digitized into 512 × 512 format and 8 bits/pixel. A square ROI was chosen and the mean and standard deviation within the region were computed. The mean value corresponds to the digital value of the video signal due to transmitted X-rays. In this measurement, the video signals were not logarithmically amplified prior to digitization.

The experiment was designed to study the amount of beam hardening due to iodine in the presence of a fixed thickness of lucite. We varied the concentration of Renografin-76 which was placed behind the lucite object. The experiment was repeated twice, using 0- and 4-mm added aluminum filtration at 70 kVp and 20 mA. The measured projection values, as defined in Eq. (16), are plotted in Figure 7. For a monoenergetic X-ray beam, i.e., $D(x,y:E) = D\delta(E - E_0)$ where E_0 is the energy, the projection given in Eq. (16) is equal to

$$\mathrm{Pr}_{\mathrm{mono}}(L) = \mu(E_0)L \tag{18}$$

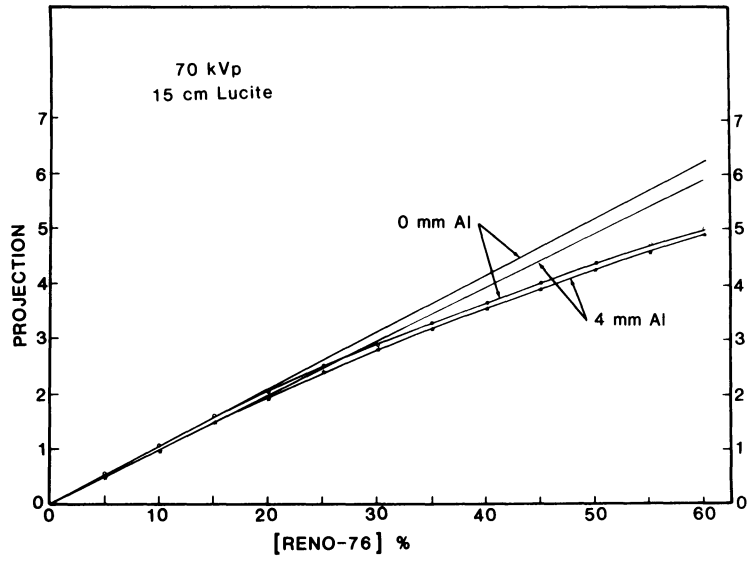

Figure 7. X-ray projection for the primary beam as a function of Renografin-76 concentration.

where $\mu(E_0)$ is the linear attenuation coefficient of a homogeneous material at an energy E_0 and thickness L (in this example, concentration). Thus, for a monoenergetic X-ray beam, the projection is a linear function of thickness. Nonlinear response in this case is due to beam hardening since the imaging system was shown previously to be linear. The straight lines in Figure 7 were obtained using the linear least-squares fitting technique with the experimental data within the low concentration range (0–5%). They also represent the monoenergetic extrapolation to the data. The deviation of the experimental points from the straight line is an indication of beam hardening with this system using iodine in the presence of 15-cm lucite. As seen from Figure 7 and as expected, the deviation is larger than 0-mm added aluminum filtration.

3.2. X-Ray Scatter

An experimental study of the effect of object scatter without the influence of veiling glare was undertaken in the following manner. A lead cover with a small circular aperture (1 cm ∅) at the center was used to cover the II face as described in Section 3.1. The lead collimators in front and back of the scatter medium were removed. The experimental setup is illustrated in Figure 8. The distance between the exit face of the lucite

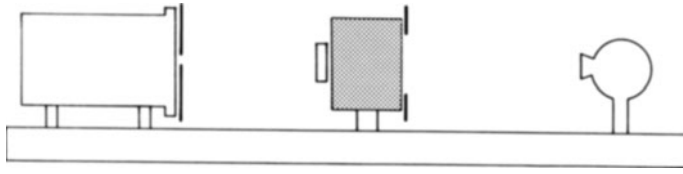

Figure 8. Open beam geometry for measuring X-ray scatter.

and II input was 25 cm. A 15-cm-diameter circular collimator was placed on the entrance face of the lucite which geometrically restricted the transmitted primary X-rays to just within the diameter of the intensifier input (9-inch diameter). With this setup, the detected video signal within the circular aperture was given by

$$V_2(x,y) = c \int D(x,y:E)N(x,y:E)dE \tag{19}$$

where N is given by Eq. (2) and includes both the primary and scattered photons detected at location (x,y). Due to removal of veiling glare with this experimental setup, we substituted $T(x,y;x',y') = \delta(x - x')\delta(y - y')$ in deriving Eq. (18) from Eq. (4). The amount of beam hardening was determined in Section 3.1 and can be corrected for, so as to eliminate beam-hardening artifacts and study the effect of X-ray scatter alone.

An experimental study of Eq. (18) was done using 15-cm lucite with various concentrations of 2-cm-thick Renografin-76 solution as discussed in Section 3.1. The video signal was measured both with and without an X-ray grid on the II. The measured signal, primary plus scatter, is denoted by P + S in Figure 9. The primary signal (P) with and without the grid was measured using the experimental setup shown in Figure 6. The scatter component (S) was computed by taking the difference of (P + S) and (P) and is also shown in Figure 9. It is seen that for large concentrations of iodine, the (P + S) curves approach a constant value asymptotically. This is due to the fact that for large concentrations of iodine, neither the primary nor the scattered photons pass through iodine. The X-rays which reach the open aperture in this case are the ones which are scattered within lucite without passing through the iodine. Thus, this scattered component is independent of the iodine concentration and hence the constant value. The total number of scattered photons reaching the open aperture on the II (see Figure 8) can be expressed as

$$S_{\text{total}} = S_{\text{iodine}} + S_{\text{outside}} \tag{20}$$

where S_{iodine} and S_{outside} are the number of scatterd photons passing through iodine and the outside region, respectively. In Figure 10, S_{iodine} was com-

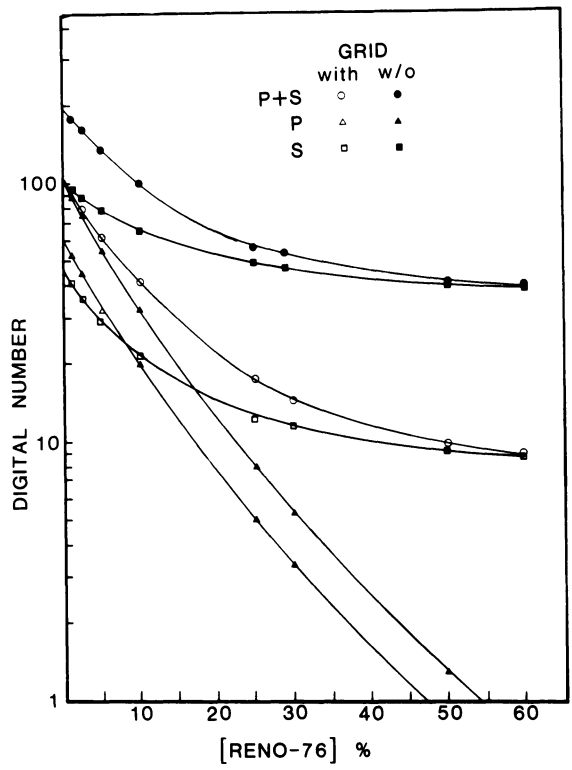

Figure 9. Measured digital numbers versus Renografin-76 concentration. P, primary; S, scatter; P + S, primary and scatter.

puted by subtracting the constant asymptotic value (i.e., for large iodine concentrations) from S_{total}. It is seen from Figure 10 that when S_{iodine} versus concentration is plotted semilogarithmically, one obtains the expected straight line relationship. The situation is similar with or without the X-ray grid. The measurements presented in Figures 9 and 10 were done with 4-mm Al added filtration at 70 kVp. Figure 11 shows the measured projection (see Eq. 16) as a function of iodine concentration. In the same figure, we plotted the polychromatic primary projection taken from Section 3.1 as well as the monoenergetic extrapolation. We see that the polychromatic projection deviates from the straight line monoenergetic one as the concentration of iodine is increased. The deviation from linearity is more substantial when the scatter is included. As one would expect, the situation is slightly better with than without the grid. The results presented in this section included the effects of scatter and beam hardening on the measured video signal and deviation from linearity of the projection.

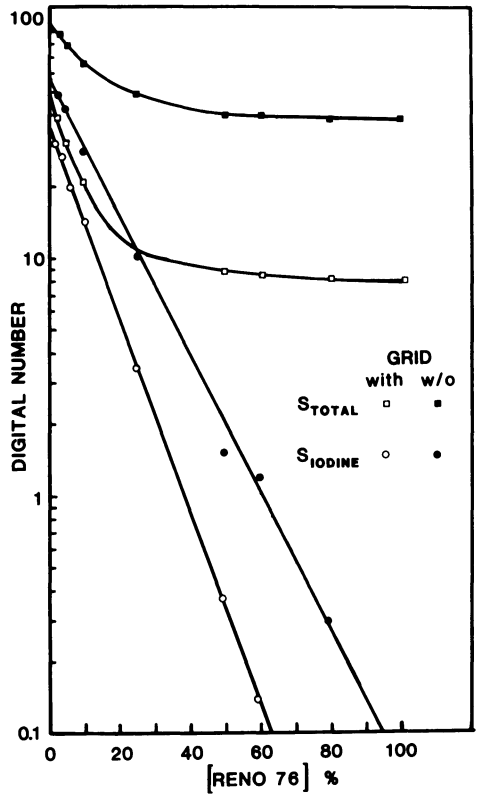

Figure 10. Computed scatter contribution versus iodine concentration.

3.3. Veiling Glare

The final study included all the physical degradation factors: beam hardening, X-ray scatter, and veiling glare. In this case, the detected video signal at a location (x,y) is given by Eq. (4). An experimental realization of this was achieved by removing the lead cover on the II, thus exposing the whole input phosphor during the experiments. The setup is illustrated in Figure 12. The experiment was performed by changing the concentration of Renografin-76 within a 2-cm-thick bottle in the presence of 15-cm-thick lucite. The images were acquired with 70 kVp at 20 mA. The experiment was repeated both with and without an X-ray grid. The mean digital number within a small square region at the center of the image was measured for all cases. These numbers, indicated by (P + S + VG), are shown with and without a grid in Figure 13. Also shown are the primary measurements performed by using the setup described in Section 3.1. The two curves for the primary with and without the grid are separated by a

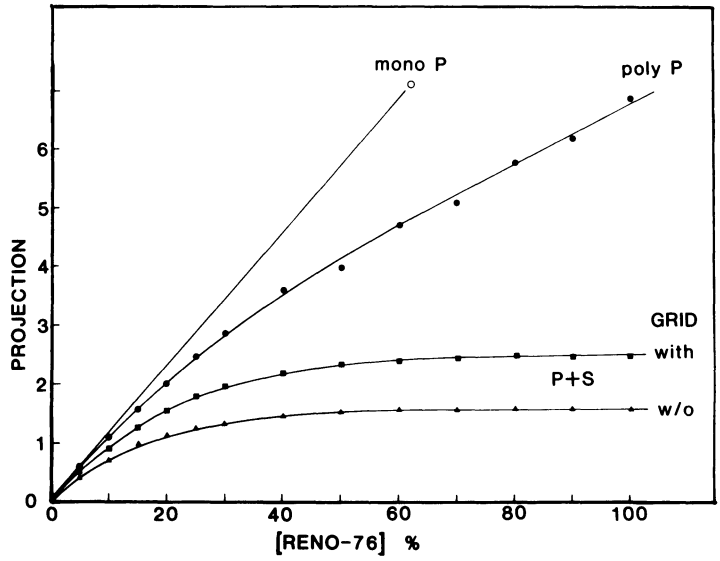

Figure 11. Projection for various cases as a function of iodine concentration.

constant amount due to constant grid transmission. The measured digital number for (P + S + VG) approaches a constant value as the concentration of Renografin-76 is increased in a manner similar to that of Section 3.2. Using the data presented in Figure 13, we computed the projection for this case. The results are shown in Figure 14. The projection for (P + S) and (P + S + VG) both become constant as the iodine concentration becomes large. Including veiling glare makes the situation a little worse. As one might expect, the use of an X-ray grid somewhat improves the overall response. In the same figure, we show the primary projection which is degraded only by beam hardening. Finally, we show the projection data with a grid for all three cases in Figure 15, and include the linear extrapolation for each case, indicated by "mono." These straight lines

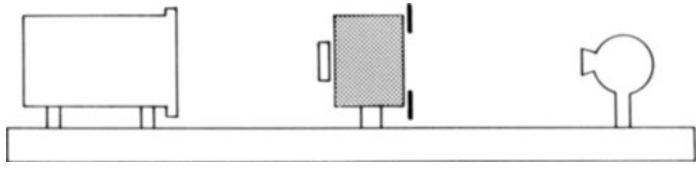

Figure 12. Open field geometry to include veiling glare, scatter, and beam hardening.

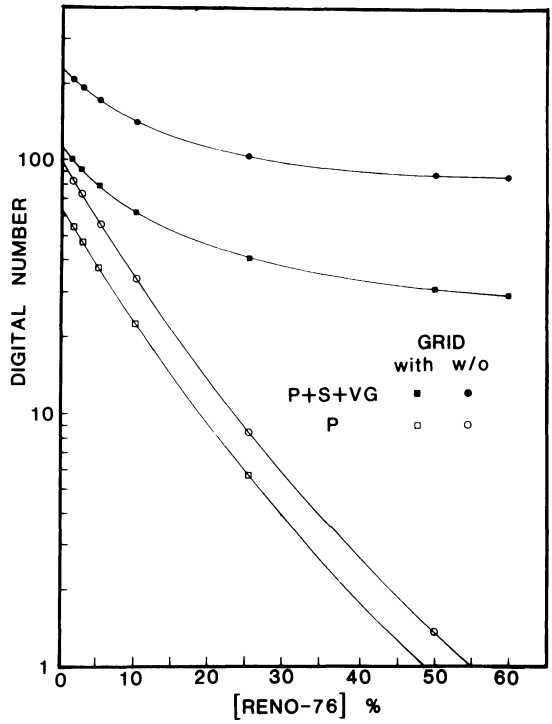

Figure 13. Measured digital numbers versus iodine concentration. P, primary; P + S + VG, all degradations included.

were obtained by fitting a straight line through the first two or three experimental points. A substantial deviation from linearity exists for all three cases. It is the nonlinearity projection data which cause errors in measurements. These errors are the subject of the next section.

4. EFFECT OF DEGRADATION FACTORS ON VIDEODENSITOMETRIC VOLUME MEASUREMENTS

An experimental investigation of the nonlinear behavior of X-ray projection as a function of object thickness was presented in Section 3. In these studies, we used a 2-cm-thick bottle filled with various concentrations of iodine and placed it behind a 15-cm-thick lucite block. By varying the experimental setup, we were able to measure the projection as a function of iodine concentration under various experimental conditions. The projection data presented in Figures 14 and 15 were for a single

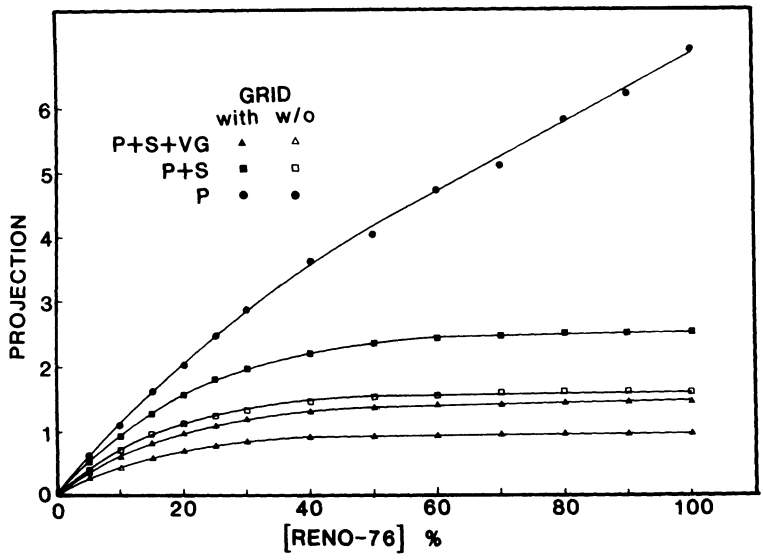

Figure 14. Projection for P, P + S, and P + S + VG as a function of iodine concentration.

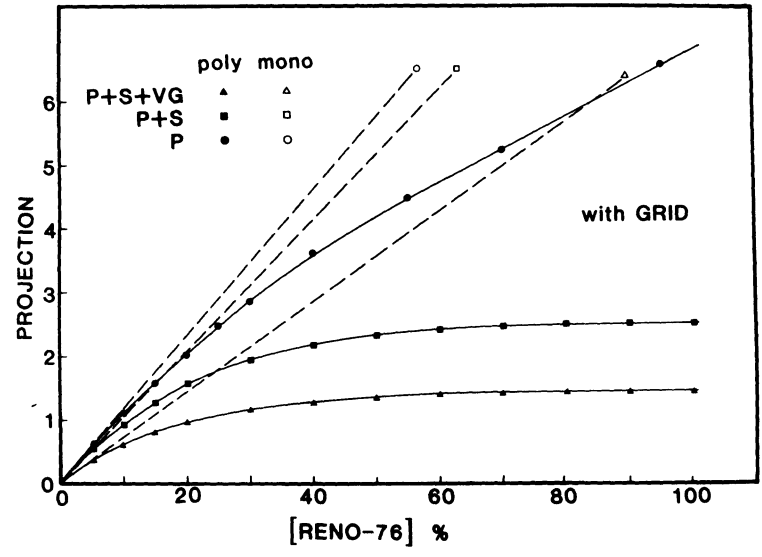

Figure 15. Projection using an X-ray grid for P, P + S, and P + S + VG (solid curves). Dashed lines are respective monochromatic extrapolations.

ray passing through the object. The experimental projection data were used in a mathematical simulation of a three-dimensional object filled with Renografin-76 under the same experimental conditions. The object chosen was an ellipsoid of revolution. The two minor axes were taken to be equal while the major-to-minor-axis ratio was assumed to be 2:1. In the first simulation, the major axis was taken to be along the X-ray beam direction (a parallel beam geometry was also assumed). This situation is clinically similar to left ventricular imaging using the left anterior oblique (LAO) view with X-rays traveling along the long axis of the ventricle. In the second situation, we assumed the X-ray beam to be perpendicular to the long axis of the ellipsoid of revolution. This view clinically represents the right anterior oblique (RAO) imaging of the left ventricle. From here on, we will call these two different simulations LAO and RAO, respectively. The simulated volume of the ellipsoid was varied from 2 to 200 cm^3 while keeping the ratio of the axes constant. All the different size ellipsoids were assumed to be filled with a 10% concentration of Renografin-76. In order to compute the gray levels within the simulated images, we first computed the cord length through the ellipsoid corresponding to a given pixel location within the image, and then assigned the experimental X-ray projection corresponding to this specific cord length to that pixel. Since the cord lengths vary continuously from one point to another within the object, the simulation requires a knowledge of the X-ray projection as a function of object thickness continuously. This was accomplished by fitting a polynomial to the experimental projection data shown in Figures 14 and 15. The specific function used is given by

$$\Pr(x) = \sum_{i=1}^{M} a_i(x)^i \tag{21}$$

where M is the order of the polynomial, x is the thickness of 10% Renografin-76, and a_i are the coefficients obtained by a least-squares fitting of Eq. (21) to the experimental data. In all studies, it was sufficient to choose $M = 4$. Two examples of the simulated ellipsoid images are shown in Figure 16. In Figure 16a is shown a simulated RAO image of the ellipsoid of revolution. The LAO image, which is in a direction perpendicular to the circular cross section, is shown in Figure 16b.

4.1. Absolute Volume Measurements

By using the experimental projection data degraded by beam hardening, scatter, and veiling glare, we studied the order of magnitude of the

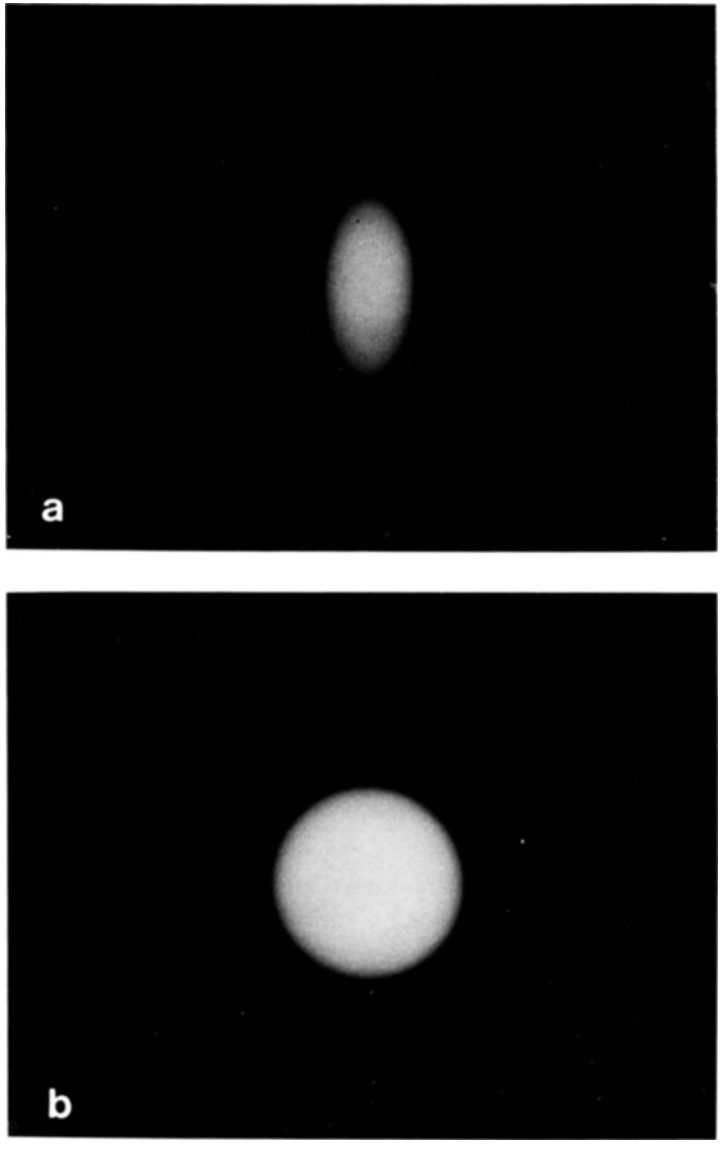

Figure 16. (a) Simulated RAO-view ellipsoid of 50-cm^3 volume (P + S with grid). (b) Simulated LAO-view ellipsoid of 50-cm^3 volume with different magnification (P + S with grid).

errors introduced by various physical degradation factors. Once a simulated image was generated, the total videodensitometric signal was measured by integrating the gray levels within the object. Figure 17 illustrates the selection of a region-of-interest (ROI) around the object. The integrated net signal within the ROI is supposed to be proportional to the volume of the object. We are now in a position to verify the correctness of this statement. In Figure 18, we show the videodensitometrically measured volume versus the actual ellipsoid volume. The monochromatic curve was obtained by fitting a straight line through the first few experimental points. This curve was also used to normalize the measured volume so that it is given in units of cm^3. As a result of the normalization, P_0 represents the line of identity. In the same figure, we also show the curves for the primary beam and the realistic case when all the degradation factors were included. The measured volumes for the RAO view using the primary beam alone are slightly underestimated, maximum being at 200 cm^3. This is due to additional beam hardening by the iodine within the ellipsoid. In the RAO view, the largest thickness is 5.8 cm for the 200-cm^3 volume (i.e., minor axis). When beam hardening, scatter, and veiling glare are all included, the deviation from the line of identity becomes larger. Notice that, in spite of this large departure from the line of identity, the curve is still fairly linear. The meaning of this observation

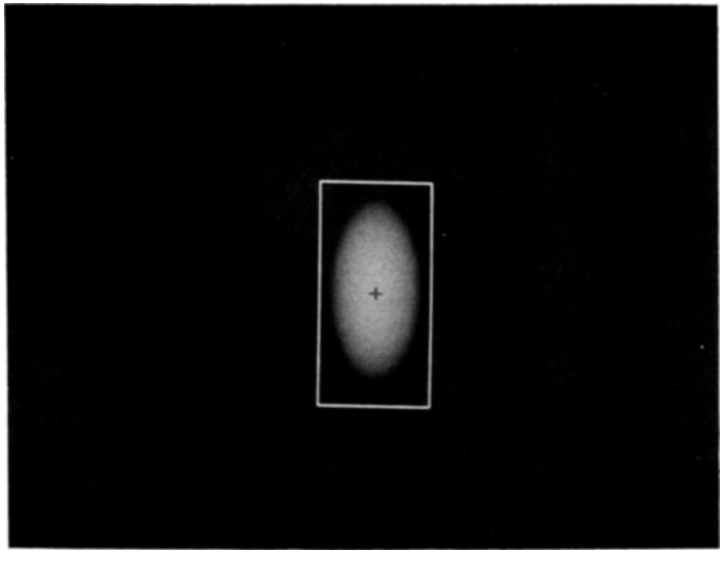

Figure 17. Selection of an ROI around the object.

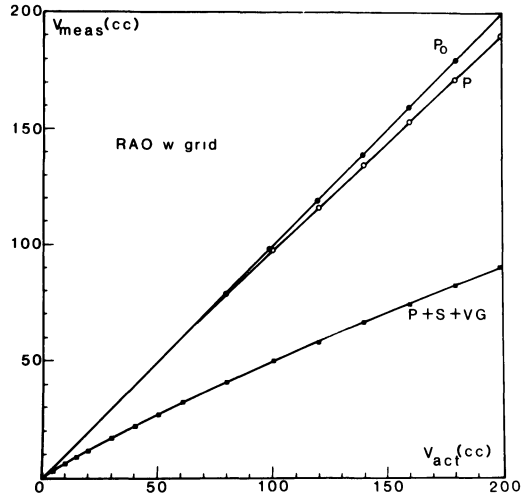

Figure 18. Measured volume versus actual one for the RAO view for various cases.

is that, while the absolute value measurements may be underestimated greatly, relative volume measurements such as ejection fraction would be underestimated less. Figure 19, representing the LAO view, shows what happens when we image the ellipsoid along the long axis. The notation is the same as for Figure 18. The underestimation of volumes obtained using the primary beam are larger than the previous (RAO) case. The largest thickness traversed in the LAO case is the major axis, 13 cm for

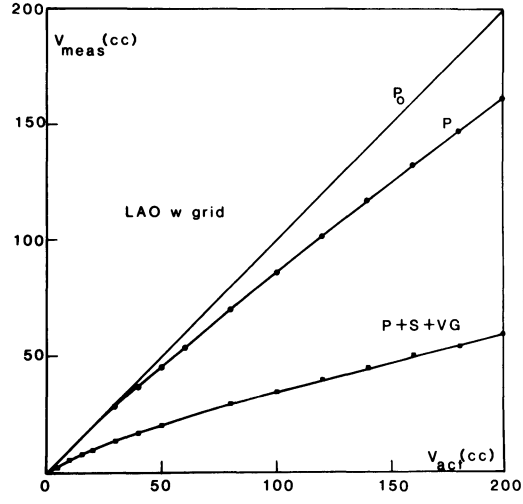

Figure 19. Same as Figure 18 but for LAO view.

the 200-cm^3 volume. Thus, we have a larger amount of beam hardening due to added iodine, and, hence, the larger deviation from the line of identity. If we study the curve obtained by using all the degradation factors, we see that it is also underestimated more as compared to the RAO case (Figure 18). However, a close examination of the curve indicates that most of this deviation is due to a larger amount of beam hardening. In other words, the separation between the primary and the full curves in Figure 19 is almost identical to that of Figure 18.

4.2. Relative Volume Measurements

In this subsection, we will define a quantity which is similar to the ejection fraction used in cardiology. It is given by

$$\mathrm{EF} = 100(1 - V_</V_>) \tag{22}$$

where $V_<$ and $V_>$ correspond to end-systolic and end-diastolic volumes, respectively. We will also define a percentage error (ϵ) by

$$\epsilon = 100[1 - \mathrm{EF(measured)/EF(actual)}] \tag{23}$$

In Figure 20, we show the percentage error in EF for two different end-diastolic volumes, i.e., for $V_> = 80$ and 200 cm^3. These curves were obtained for the case when all the degradation factors were included. In the RAO view, the largest percentage error occurs for large end-diastolic volumes with small ejection fractions. Intermediate, end-diastolic error

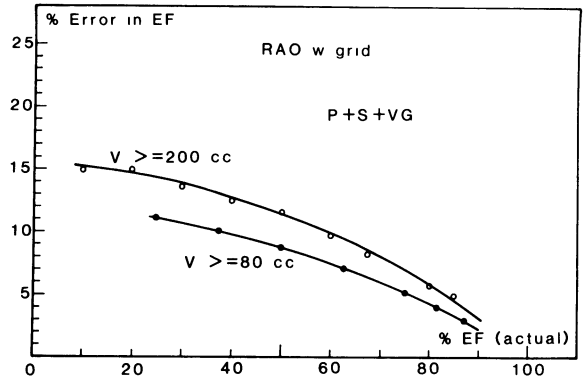

Figure 20. Percentage error in EF as a function of actual EF and various end-diastolic volumes—RAO view.

curves lie in between the two shown in Figure 20. It is seen from Figure 20 that for an ejection fraction of 70% and an end-diastolic volume of 200 cm^3, the error is 8%. If the actual ejection fraction is 30% for the same end-diastolic volume, the error goes up to 14%. The results shown in Figure 20 were obtained for the RAO view. Similar results for the LAO view are shown in Figure 21. Here, the errors are slightly larger compared to the RAO case.

5. TECHNIQUES FOR REDUCTION OF DEGRADATION FACTORS

In this section, we will discuss and review some techniques for improving the accuracy of measurements performed with digital fluoroscopic systems. The degradation factors which will be considered are the ones mentioned in the previous sections, namely beam hardening, X-ray scatter, and veiling glare.

5.1. Veiling Glare

The equation which describes the relationship between the incident X-ray flux and the output video signal is given by

$$V(x,y) = \beta \iiint D(x',y':E)T(x,y;x',y')N(x',y':E)dx'dy'dE \tag{24}$$

where we assumed that a plumbicon TV camera with $\gamma = 1$ is used. Using the Seibert model,[14] we will expand T in terms of a function h, which is the stationary point spread function (PSF),

$$T(x,y;x',y') \simeq h(x - x', y - y') + \Delta h \tag{25}$$

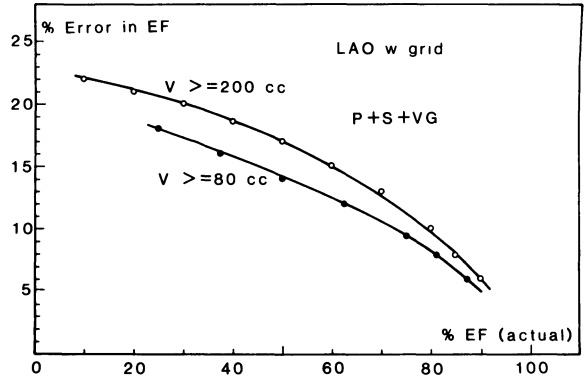

Figure 21. Same as Figure 20 but for LAO view.

where Δh represents higher-order nonstationary terms. We have shown earlier that Δh is negligible compared to h.[14] In other words, PSF depends only on the difference of and not on each variable separately. This allows rewriting of Eq. (25) as a convolution relationship which is given by

$$V(x,y) = [h**U]_{(x,y)} \tag{26}$$

where $**$ is a two-dimensional convolution operation and U is the image which is not degraded by the TV–II system. It is defined by

$$U(x,y) = \beta \int N(x,y:E)D(x,y:E)dE \tag{27}$$

A derivation of the veiling glare PSF was outlined in a previous publication.[15] This derivation was based on the assumption of linear system response, circular symmetry, and spatial invariance of the II PSF. It was shown that the theoretical PSF can explain the experimental results to a high degree of accuracy. The analytical form of PSF is given[12] as

$$h(r) = (1 - \rho)\,\delta(r)/r + \rho \exp(-r/k)/(2kr) \tag{28}$$

where ρ and k are the parameters describing the fraction of strongly scattered light and its mean propagation distance, respectively. The symbol δ in the above equation is the Dirac delta function. The relationship between the undegraded image, $U(r,\theta)$, and the actual detected image, $V(r,\theta)$, in polar coordinates is given by

$$V(r,\theta) = [h**U]_{(r,\theta)} \tag{29}$$

Equation (29) mathematically represents the two-dimensional (2D) convolution of the II PSF $[h]$ with the undegraded image $[U]$ resulting in the detected image $[V]$. In this equation, $**$ represents the 2D convolution process, and (r,θ) the polar coordinate system chosen with which to describe the process. The PSF $[h]$ is represented as a linear and rotationally symmetric function. Thus, we neglect the higher-order terms expressing the nonlinear and nonstationary system response based on our previous findings.[15]

The 2D convolution in spatial domain given in Eq. (29) can be represented in the frequency domain by

$$F_2[V] = F_2[U]\,F_2[h] \tag{30}$$

where $F_2[\cdot]$ is a 2D FT operation. The right-hand side of Eq. (30) is a multiplication of the frequency domain representation of the undegraded

image with the PSF on a point-by-point basis. Inverting $F_2[h]$ in Eq. (30) and taking the inverse FT yields

$$U(r) = V(r) ** F_2^{-1} \tag{31}$$

where $F_2^{-1}[\cdot]$ is the inverse 2D FT operation. The undegraded image U can be obtained by direct 2D deconvolution on the acquired spatial domain image with an inverse filter[16] if the PSF $[h]$ is known.

The spatial extent of the veiling glare PSF is considerable, as indicated by the magnitude of k. The mean value is typically 2–3 cm, while the pixel size has millimeter dimensions. In order to properly deconvolve the PSF, a large number of pixels becomes mandatory to fully describe the inverse filter. The long range of the filter prohibits the implementation of Eq. (31) in the spatial domain due to the excessive computation time required. Instead, the efficiency and speed of the fast Fourier transform[17] permits rapid deconvolution to be carried out in the frequency domain by solving for $F_2[U]$ in Eq. (30) and inverse transforming the result:

$$U = F_2^{-1}[F_2[V] \{1/F_2(h)\}] \tag{32}$$

Since we know the analytical form of h, $1/F_2[h]$ can also be analytically derived, with the tremendous benefit of avoiding singularities and oscillatory behavior present in a digital calculation caused by finite sampling width, truncation errors, and problems associated with noise.

The veiling glare PSF can be transformed into the frequency domain by Fourier methods:

$$\hat{H}(f) = \int_0^{\infty} \int_0^{2\pi} h(r)\, e^{-2\pi i \mathbf{r}\cdot\mathbf{f}}\, r dr d\theta \tag{33}$$

In this equation, f is the spatial frequency (cm^{-1}) and $\hat{H}$ is the frequency domain representation of h. Taking advantage of the circular symmetry, the Fourier transform becomes a Hankel transform, giving

$$\hat{H}(f) = 2\pi \int_0^{\infty} h(r) J_0(2\pi r f) r dr$$

and substituting Eq. (28) results in

$$\hat{H}(f) = 2\left[\frac{\rho}{2k}\int_0^{\infty} e^{-r/k} J_0(2\pi r f) dr + (1-\rho)\int_0^{\infty} \delta(r) J_0(2\pi r f) dr\right] \tag{34}$$

where J_0 is the zero-order Bessel function and δ is the Dirac function.

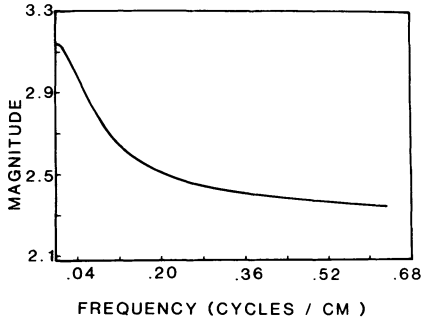

Figure 22. Veiling glare PSF in the frequency domain.

Integrating and solving Eq. (34) results in the frequency domain PSF

$$\hat{H}(f) = \Pi\left[\frac{\rho}{\sqrt{1 + (2\pi kf)^2}} + (1 - \rho)\right] \tag{35}$$

The form is illustrated in Figure 22. Only a profile along a radius is shown. The complete filter may be obtained by rotating about the z axis.

Inversion of Eq. (35) gives the solution of the inverse frequency filter

$$\hat{H}^{-1}(f) = \frac{1}{\pi}\left[\frac{\sqrt{1 + (2\pi kf)^2}}{\rho + (1 - \rho)\sqrt{1 + (2\pi kf)^2}}\right] \tag{36}$$

Its form is plotted in Figure 23. As illustrated, the filter is essentially high pass in nature; it retains higher frequencies, and selectively attenuates lower frequencies which contribute to the veiling glare degradation in the image.

Multiplication of this filter on a point-by-point basis with the frequency domain degraded image yields a product in the frequency domain

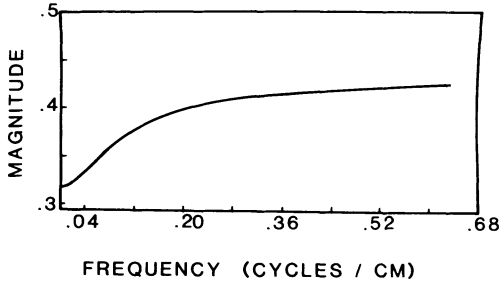

Figure 23. Inverse filter in the frequency domain.

that has the lower frequencies deamplified. Application of an inverse 2D FT with appropriate scaling factors results in an approximate estimate of the original undegraded image. The spatial domain representation of the inverse filter with values of $\rho = 0.28$ and $k = 2.7$ cm is illustrated in Figure 24. The graph indicates the negative contribution of values to the point being deconvolved, counteracting the spread of light at adjacent pixels. The spatial extent of the filter is extensive, with significant negative weighting at large distances from the center pixel.

5.1.1. Deconvolution of Lead Disk Images

A lead disk of 1/8-inch thickness was placed on the II input phosphor cover (no grid) and a digital fluoroscopic image was acquired. The focal spot to input phosphor distance was 1.5 m. No scattering medium was present. The image is shown in Figure 25a. Notice that even though the lead disk was thick enough to stop any X-ray transmission through it, the

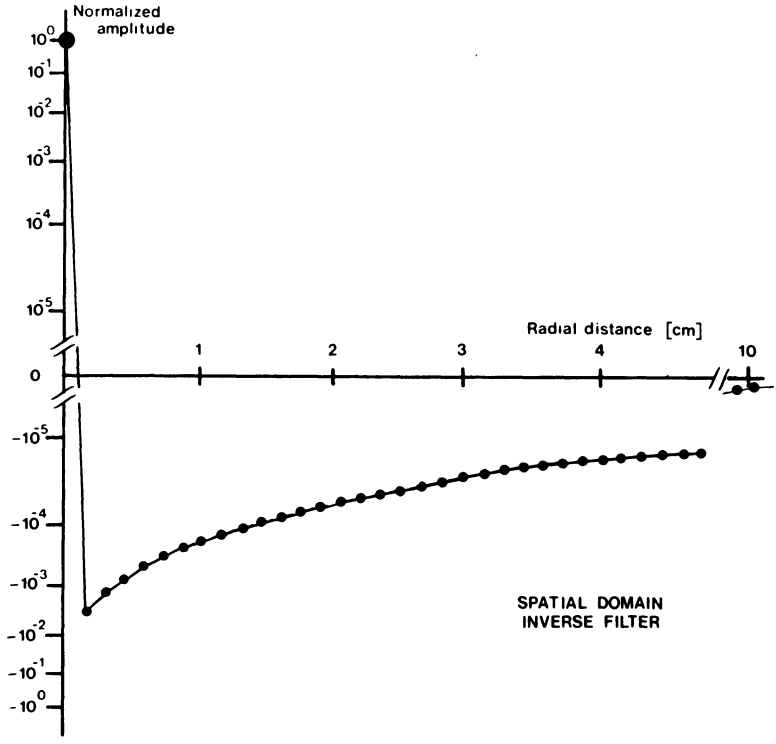

Figure 24. Normalized inverse filter in the spatial domain.

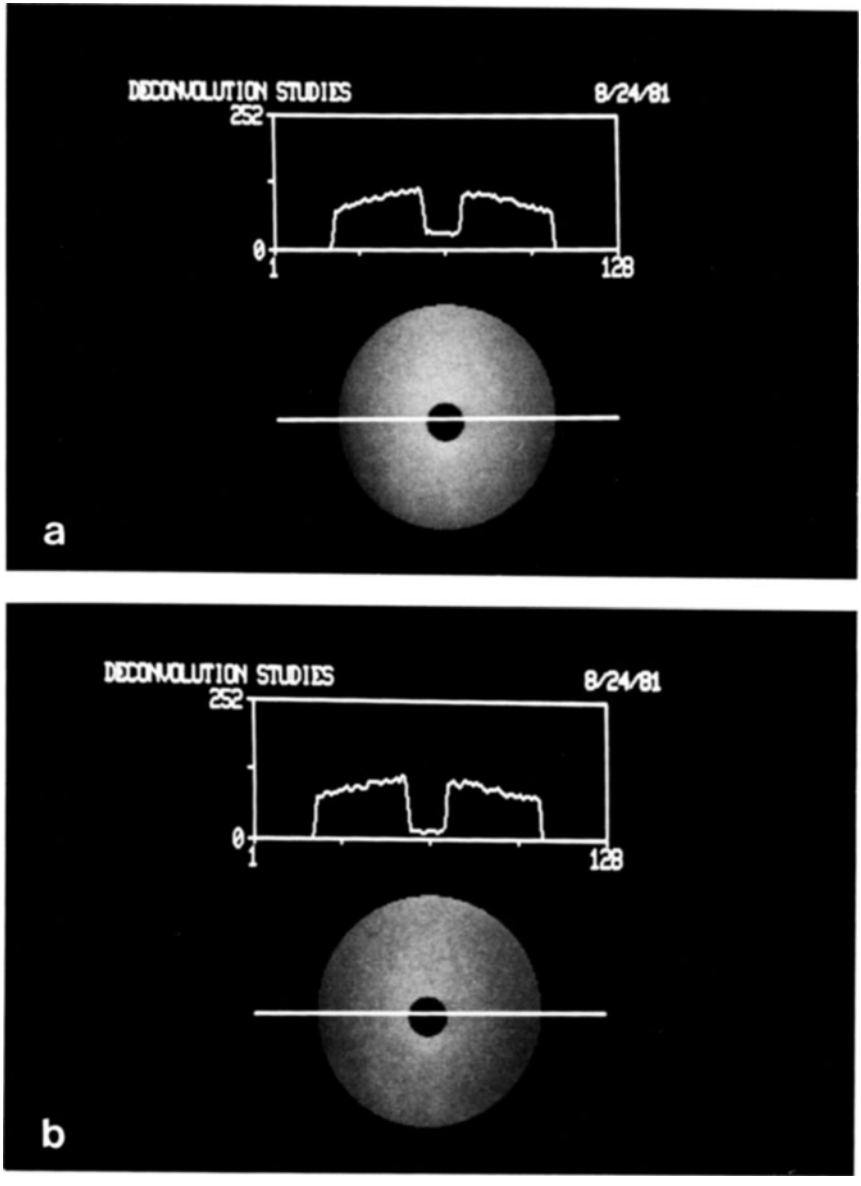

Figure 25. (a) A lead disk image and a diametric profile without deconvolution. (b) Same image after glare deconvolution.

video profile displayed in Figure 25a indicates a nonzero reading under the lead disk. This is due to the glare effect under discussion all along. The light produced within the open areas leads into the region which is covered by the disk. After applying the glare deconvolution technique discussed in Section 5.1, we obtained the deconvoluted image shown in Figure 25b. The signal under the lead disk is close to zero. If the deconvolution process were to be totally accurate, we could have obtained a zero reading under the disk.

5.1.2. Effects of Glare Deconvolution on Volume Measurements

In Section 5.1.1, we studied the effect of veiling glare deconvolution in the absence of any scatter medium. We will now discuss what happens when a scatter medium is present. Furthermore, we will also investigate what happens to volume measurements. We used the images of the iodine bottle filled with different concentrations of Renografin-76 and placed behind a 15-cm-thick lucite phantom. As mentioned earlier, all three of the physical degradation factors we have been concerned with were present in these images. We deconvolved each image (containing different concentrations of iodine) with the appropriate veiling glare filter and computed the X-ray projection again. These results are shown in Figure 26. Here, the projections for the primary beam, primary plus scatter, and primary plus scatter plus veiling glare are shown. For comparison, we

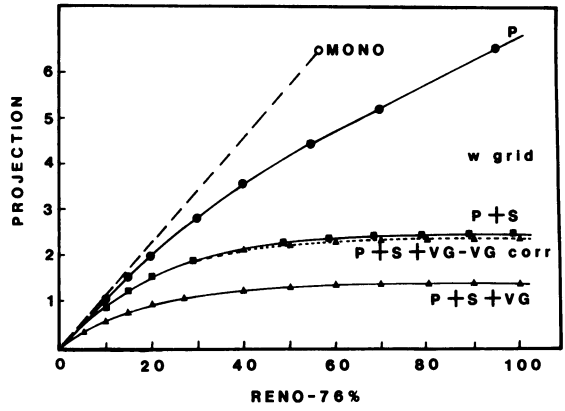

Figure 26. Summary of projection versus concentration of Renografin-76 for primary (P), primary plus scatter (P + S), and primary plus scatter plus veiling glare (P + S + VG) polychromatic projections and their monoenergetic extrapolations. Also shown are the deconvolved projection data using an inverse PSF: $\rho = 0.241$, $k = 2.97$ cm as measured for the II used in the experiments (small dashed curve, veiling glare corrected).

also indicate the projection obtained after deconvolution of the veiling glare PSF. The deconvolution process brings the (P + S + VG) projection curve almost on top of the (P + S) one. For perfect deconvolution, (P + S) and "VG corrected" curves should overlap. It is seen from Figure 26 that the projection obtained after glare deconvolution does not contain much glare effect.

We used deconvolved projection data and studied the effect of the glare reduction technique on videodensitometric absolute volume measurements. In this investigation the "LAO" ellipsoid of revolution phantom discussed in Section 4.1 was used. The results are shown in Figure 27. It is seen that the experimentally obtained (P + S) curve and the mathematically obtained one, i.e., deconvolved (P + S + VG) curve, almost overlap. Thus, we conclude that the deconvolution technique discussed in Section 5.1 is quite good in reducing the errors introduced by veiling glare.

5.2. X-Ray Scatter

We saw in the last section that after the deconvolution of veiling glare, we are left with the system undegraded image U which was defined by Eq. (27). The function N used in Eq. (27) was defined in Eq. (2) as

$$N(x,y:E) = P(x,y:E) + S(x,y:E) \tag{2}$$

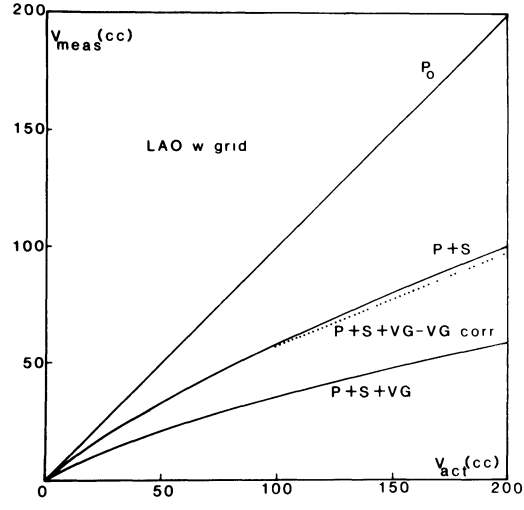

Figure 27. Measured volume versus actual one for the cases shown in Figure 26.

where P and S are the primary and scattered photons incident on the II, respectively.

As we have seen in Section 3.2 (Figure 10), some fraction of the scattered photon distribution may appear as a low-frequency version of the primary photon distribution, i.e., carries some information about the spatial distribution of attenuators within the object. Mathematically, we can express this as

$$N(x,y:E) = \int P(x',y':E)h_s(x - x',y - y':E)dx'dy' \tag{37}$$

where the scatter PSF is defined by

$$h_s(x,y:E) = \delta(x)\delta(y) + \left[\frac{s(x,y:\epsilon)}{p(x,y:\epsilon)}\right] g(x,y:\epsilon) \tag{38}$$

In Eq. (38), $\delta(\cdot)$ is a one-dimensional delta function and $g(x,y:E)$ is a function to be determined later. We also notice that the quantity in brackets is the scatter-to-primary ratio (SPR). We will now approximate the SPR by

$$\text{SPR} \simeq S(0,0:\bar{E})/P(0,0:\bar{E}) \tag{39}$$

where $\bar{E}$ is the effective beam energy for the X-ray beam. We can now rewrite Eq. (38) as

$$h_s(x,y:E) = \tilde{h}_s(x,y:\bar{E}) + \Delta h_s \tag{40}$$

where

$$\tilde{h}_s(x,y:\bar{E}) = \delta(x)\delta(y) + \text{SPR} \cdot g(x,y:\bar{E}) \tag{41}$$

We also substituted $\bar{E}$ for E in g. As a first-order approximation, we will now assume that Δh_s in Eq. (40) is small compared to $\tilde{h}_s$. Thus, we can rewrite Eq. (38) as

$$N(x,y:E) \simeq \int P(x',y':E)h_s(x-x',y-y':\bar{E})dx'dy' \tag{42}$$

The last term in Eq. (41) is similar to the scatter PSF as defined by Barrett and Swindell.[18] They have shown that in the single-scatter approximation,

$$g_{\text{single}}(r:\bar{E}) = \exp[-\alpha(\bar{E})r^2] \tag{43}$$

where α is an energy-dependent coefficient. If one takes multiple scattering into account, Eq. (43) can be generalized into

$$g_{\text{multi}}(r:\bar{E}) = \exp[-\alpha(\bar{E})r^2] \sum_{i=1}^{M} \beta_i(\bar{E})(r)^{2i} \tag{44}$$

where M is the number of terms in the expansion and $\beta_i(\bar{E})$ are energy-dependent coefficients. Equations (43) and (44) indicate that for a thin object ($M = 0$), the scatter PSF is a Gaussian. For thicker objects, multiple scattering becomes significant and one has to use the more general formula given in Eq. (44). The higher-order terms make the Gaussian function broader, indicating a less structured two-dimensional scattered photon distribution. This, of course, is intuitively correct since the directional information the scattered photons carry is lost as a result of multiple scattering. If we substitute Eq. (42) in Eq. (27), we obtain

$$U(x,y) = (P{**}\tilde{h}_s)_{(x,y)} \tag{45}$$

where

$$\tilde{P}(x,y) = \int P(x,y:E)D(x,y:E)dE \tag{46}$$

Thus, if h_s is known, we can compute P by deconvolving U with the inverse filter in a similar fashion to the veiling glare case. It should be noted that the overall video image $V(x,y)$ can also be rewritten as

$$V(x,y) = h_{VG}{**}(h_s{**}P)_{(x,y)} \tag{47}$$

where h_{VG} is the veiling glare PSF discussed in the previous section. Since the convolution operations commute, the equation can also be expressed as

$$V(x,y) = [P{**}(h_{VG}{**}h_s)]_{(x,y)} \tag{48}$$

The expression given in Eq. (48) indicates that if h_{VG} and h_s are known, they can be convolved to yield a two-dimensional overall PSF which can then be used to compute $P(x,y)$, the image which is degraded by beam hardening alone.

An earlier work performed by Shaw *et al.*[11] utilized an overall inverse filter which is given by

$$f(x,y) = \delta(x)\delta(y) - C\,{}^2\Pi(ax,ay) \tag{49}$$

where ${}^2\Pi(ax,ay)$ is a two-dimensional rectangle function[19] which is defined by

$$ {}^2\Pi(ax,ay) = \begin{cases} 1 & |x|,|y| \leq 1/2a \\ 0 & \text{elsewhere} \end{cases} \tag{50} $$

In Eq. (49), C is a constant to be adjusted. The application of the filter defined in Eq. (49) results in the high pass filtering operation of the degraded video image $V(x,y)$. Even though the filter used by these investigators[11] was quite arbitrary, it has been shown that the deconvolution of f linearizes the nonlinear videodensitometric volume curve quite successfully.

To conclude this section, we will simply state that the deconvolution techniques appear to be promising for obtaining accurate videodensitometric data. Current research at the University of California, Irvine, is focused on the determination of h_s and experimental validation of the approximations made in the development of the formalism.

5.3. Beam Hardening

In this subsection, we will assume that two correction techniques discussed in Sections 5.1 and 5.2 have been successfully applied to the acquired images. Thus, the processed images would only be affected by the beam-hardening artifacts discussed earlier. An obvious method for reducing the effect of beam hardening is to prefilter the X-ray beam heavily so that the X-ray beam becomes quasi-monoenergetic. The most common filters used for this purpose are aluminum or copper. Even though filtration of the X-ray beam reduces the beam-hardening effects, it also results in an increase in the quantum noise within the images. Thus, excessive filtration may prove to be undesirable since we cannot increase the X-ray tube output indefinitely. The approach which will be discussed in this section is a combination of tube filtration and the use of a lookup table. Since both veiling glare and X-ray scatter have been reduced by the use of methods discussed in Sections 5.1 and 5.2, we will only be dealing with the polychromatic primary X-ray beam. The polychromatic video signal given in Eq. (17) can be rewritten more explicitly as

$$ V(x,y) = \beta \int D(x,y:E) N_0(x,y:E) \exp\left[-\int \mu(x,y,z:E)dz\right] dE \tag{51} $$

where we assumed a parallel X-ray beam propagating along the z direction. The X-ray projection Pr at a location (x,y) can be written as

$$ \Pr(x,y:L_T,L_I) = \ln[V(x,y:L_T,L_I = 0)/V(x,y:L_T - L_I,L_I)] \tag{52} $$

In Eq. (52), it was assumed that we have a tissue thickness of L_T and $L_T - L_I$ before and after iodine injection. The detailed form of Eq. (52) is given by

$$\Pr(L_T, L_I) = \ln [I_0/I] \tag{53}$$

with

$$I_0 = \int dE\, D(E)\, N_0(E) \exp[-\mu_T(E) L_T] \tag{54a}$$

and

$$I = \int dE\, D(E)\, N_0(E) \exp\{-\mu_T(E) L_T - [\mu_I(E) - \mu_T(E)] L_I\} \tag{54b}$$

In Eqs. (53) and (54), we suppressed the dependence on (x,y) and μ_T, μ_I are the linear attenuation coefficients for tissue and iodine, respectively. In the monoenergetic limit, i.e., $N_0(E) = N_0 \delta(E - E_0)$, Eq. (53) reduces to the more familiar form

$$\Pr_{\text{mono}}(L_T, L_I) = [\mu_I(E_0) - \mu_T(E_0)] L_I \tag{55}$$

In Figure 7, the polychromatic projection, Eq. (53), was plotted for two different tube filtrations. It should be noticed that in Eqs. (53) and (54), the constant amount of tissue along the beam acts as additional tube filtration, thus reducing the beam-hardening errors. This is similar to the constant-path water bath method which was used in the first-generation CT scanners.[20] We also notice that in the case of mask-subtracted videodensitometry, the projection given in Eq. (53) does not depend strongly on the tissue thickness L_T. In the monochromatic limit, there is no dependence on L_T. In order to generate a lookup table, we measured the primary projection using 4-mm aluminum filtration, 20 mA at 70 kVp. During various measurements, we used a different amount of "tissue" material and varied the concentration of 2-cm-thick Renografin-76. Some of the constant "tissue" materials experimentally used were: 0-cm lucite, 15-cm lucite, and 10-cm lucite plus 1-cm aluminum. The average polychromatic projection as a function of percent iodine concentration is given in Figure 28. It is observed that use of different types of tissue background material does not cause a significant spread in the projection data, i.e., the error bars for various concentrations of Renografin-76. The dashed straight line in Figure 28 was obtained by connecting the first three points. It represents the monochromatic projection given in Eq. (55). In order to

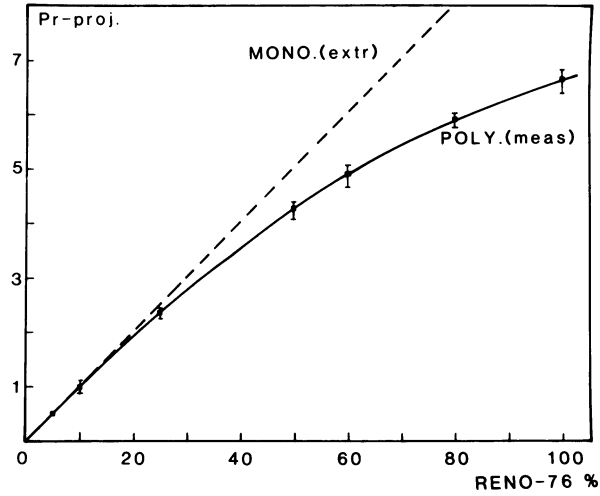

Figure 28. Measured polychromatic average projection used in the lookup function and extrapolated monochromatic projection as a function of iodine concentration.

make the experimentally measured projection data monochromatic, a transformation function was defined by

$$\text{Pr(mono)} = \sum_{j=1}^{M} a_j[\text{Pr(poly)}]^j \tag{56}$$

The coefficients a_j were determined by a least-squares fitting of Eq. (56) to the data shown in Figure 28. When $M = 5$ was used, i.e., a fifth-order polynomial, the coefficients shown in Table 2 were obtained. The lookup function obtained by using the five coefficients given in Table 2 is shown in Figure 29. Any polychromatic projection measurement along the ab-

TABLE 2. Coefficients of Lookup Function (Eq. 56)

j	a_j
1	1.375
2	−0.828
3	0.511
4	−0.109
5	0.774×10^{-2}

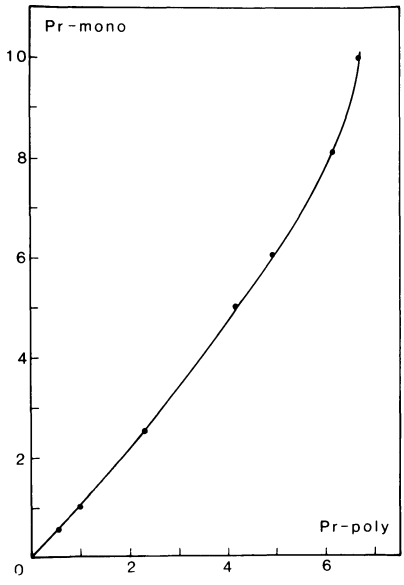

Figure 29. Monochromatic projection versus polychromatic one for 4-mm aluminum filtration, i.e., lookup function.

scissa may be converted to a monochromatic one by using Eq. (56) or Figure 29. The deviation from linearity in Figure 29 occurs more often for large values of Pr(poly). We used the experimental primary projection data which were discussed in an earlier section, and mathematically simulated the ellipsoid images as before. Each image was corrected, pixel by pixel, using the lookup function defined in Eq. (56). The measured volumes before and after the correction for LAO-view ellipsoids filled with 10% Renografin-76 are shown in Figure 30. The application of the lookup function (Eq. 56) with the coefficients given in Table 2 seems to improve the accuracy of volume measurements substantially. We should emphasize that the correction method discussed here is only applicable to volume measurements using a contrast agent since it is based on the presence of a constant thickness of background tissue and the displacement of blood by a contrast agent. The lookup function has to be precalculated using various thicknesses of tissue with the same amount of tube filtration that would be used in actual studies. Even though the correction appears to work well, the actual amount of correction would depend on the specific case under study.

6. APPLICATIONS

It was shown in the previous sections that measurements performed using II–TV-based digital X-ray imaging suffer from various degrees of

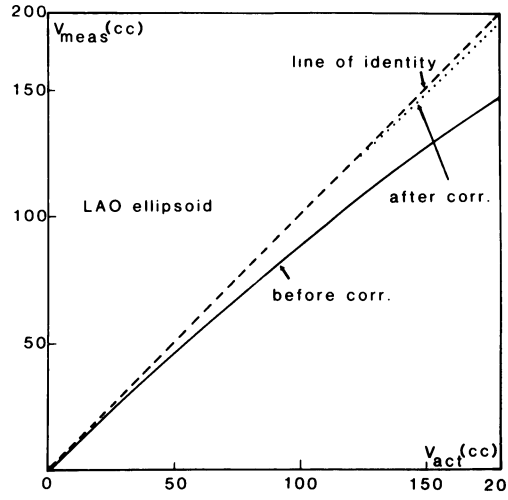

Figure 30. Measured versus actual volume of LAO ellipsoids before and after beam-hardening correction (simulation study).

errors due to the problems discussed earlier. In this section, applications regarding absolute and relative volume measurements without any correction techniques will be discussed.

6.1. Relative Volume Measurements

Here again, we will subdivide the subject into two areas. The first area will be the measurement of relative volumes of small objects. An important medical application is in the measurement of percent stenosis of vessels. The second application will be in the determination of larger relative volumes. In this case we will be concerned with the measurement of ejection fraction. The reason for dividing the applications into small and large volumes is shown in Figure 31. The actual volume of a balloon filled with 10% Renografin-76 is along the horizontal axis. The vertical axis is the videodensitometrically measured volumes in cubic centimeters. The normalization factor for actual volumes along the y axis was obtained by using the two lowest data points. The images were obtained at 70 kVp with 4-mm aluminum filtration and an X-ray grid. An interesting observation which can be made from Figure 31 is that even though the experimental curve deviates from a straight line, in two asymptotic regions there appears to be some linear response. These are marked with dashed lines in the figure. A similar observation was made by Shaw *et al.*[11] We notice that for small volumes (Region I), i.e., less than 40 cm^3, the curve appears to be a straight line with a zero intercept. However, in the second

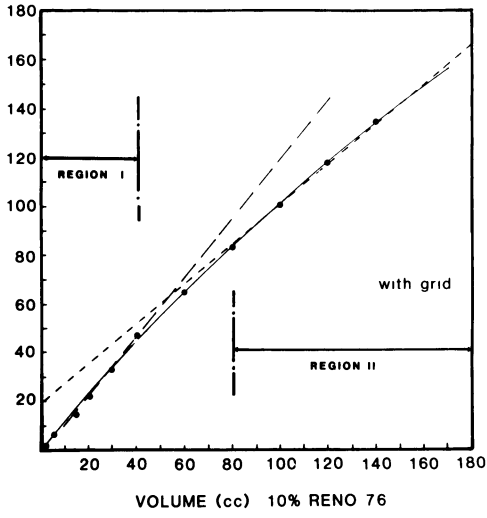

Figure 31. Measured versus actual volume of balloons filled with 10% Renografin-76 solution. Regions I and II are discussed in the text.

region, i.e., volumes larger than 80 cm^3, despite the fact that the curve seems to be a straight line, it has a nonzero intercept indicating that the measured volumes are systematically underestimated. As a result of these two linear regions, we predict that measurements done with small volumes would not suffer substantially from the errors mentioned earlier. The projection data presented in earlier sections also support this prediction. Thus, if one is interested in measuring small volumes such as vessels, one does not have to worry about applying the correction methods discussed in Section 5. However, if we were to perform measurements in Region II, the measured volumes would be underestimated by varying amounts. In order to determine the correct volumes, we would have to apply corrections to the acquired data. Even though we have identified two regions of linearity, it should be understood that the actual limits of these regions may vary depending on the experimental conditions. As a rule of thumb, for small volumes such as stenosis determination, one does not have to worry about corrections. On the other hand, the computation of ventricular ejection fraction (i.e., large volumes) would necessitate the correction of data prior to measurements.

6.1.1. Measurement of Ventricular Ejection Fraction

Percent of ejection fraction (EF) is defined as

$$\% \text{ EF} = 100(1 - V_{ES}/V_{ED}) \tag{57}$$

where V_{ED} and V_{ES} are the end-diastolic and end-systolic volumes. The computation of EF was done using the uncorrected images of balloons filled with 10% Renografin-76. The data collection was performed as follows. A mask image of the anthropomorphic chest phantom[21] was taken and stored in the computer memory. Another image was taken of a balloon filled with 10% Renografin-76 placed within the chest cavity. Two images were logarithmically subtracted without any other corrections. The process was repeated for balloons of different volumes. A sample subtracted image is shown in Figure 32. An ROI covering the object was drawn and the gray levels within the ROI were summed. The integrated value of gray levels is supposed to be a number proportional to the value of iodine mixture within the balloon. The points in Figure 31 were obtained by using these data. In order to compute various values of EF, several end-diastolic values were chosen and volumes smaller than that taken to be end-systolic volumes. The results for three different values of ED volumes are shown in Figure 33. As predicted earlier, most of the measured values are less than the actual ones. For comparison, we also show the line of identity in Figure 33. The amount of errors in this case appears to be less than that for the results presented in Section 4.2. The reason for the discrepancy is due to subtraction of a second background from logarithmically subtracted images. The secondary background in this case was chosen to be the difference between ED and ES ROIs, e.g., see Figure 34 for V_{ED} = 160 cm^3 and V_{ES} = 80 cm^3. The second background subtraction results in the cancellation of some of the errors in an arbitrary way. Similar results were reported by us earlier.[6]

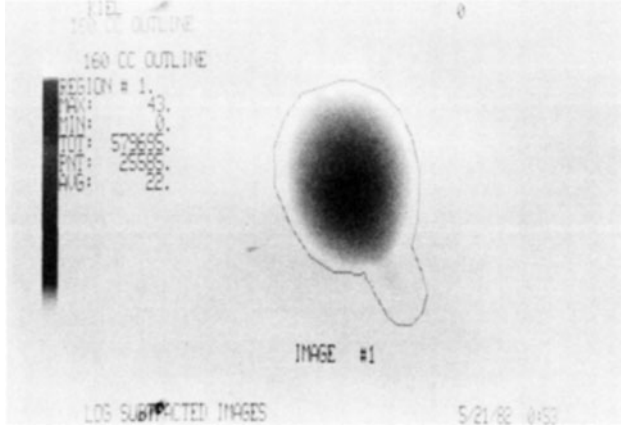

Figure 32. Selection of an ROI around 160-cm^3 balloon for volume measurement.

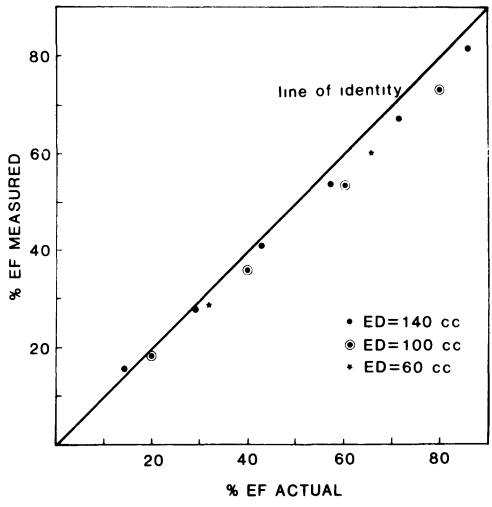

Figure 33. Measured versus actual percent EF using the balloon data.

6.1.2. Stenosis Measurement

The percent area stenosis is defined as

$$S_A = 100(1 - A_s/A_p) \tag{58}$$

where A_s and A_p are the cross-sectional areas of the stenotic and patent vessels, respectively. The data collection was performed by acquiring a

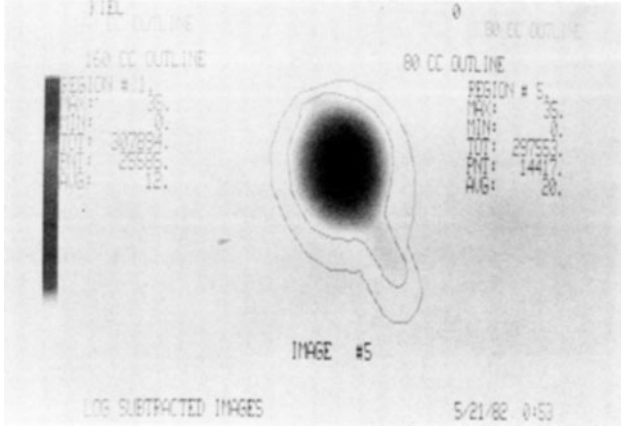

Figure 34. Selection of an ROI for secondary background subtraction.

mask image of the chest phantom. A second image containing the chest phantom and a Plexiglas block with drilled holes in it was taken. The holes had diameters ranging from 2 to 4.5 mm with 0.5-mm increments and were filled with 100% Renografin-76. The X-ray tube was operated at 75 kVp. After logarithmically subtracting the mask image from the one containing iodine, a rectangular ROI perpendicular to the midline of the patent section was chosen. The integrated digital numbers within the patent region I_p is given by

$$I_p = kV_p = kH_pA_p \tag{59}$$

where k is a constant of proportionality, H_p and A_p are the height of the ROI and cross section of the patent segment, respectively. In writing Eq. (59), we used the fact that volume $V_p = H_pA_p$. Similarly for the stenotic region, the integrated stenotic signal I_s is given by

$$I_s = kV_s = kH_sA_s \tag{60}$$

The computation of S_A is done by substituting Eqs. (59) and (60) in Eq. (58), thus resulting in

$$S_A = 100[1 - (I_sH_p/I_pH_s)] \tag{61}$$

The computation procedure is shown in Figure 35. The measured versus actual percent area stenosis is shown in Figure 36. It is seen that the largest errors occur for small values of S_A, i.e., normals where it is not

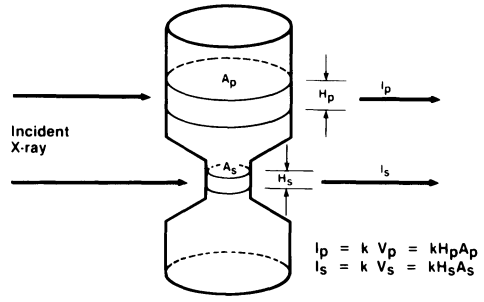

Figure 35. Stenosis measurement.

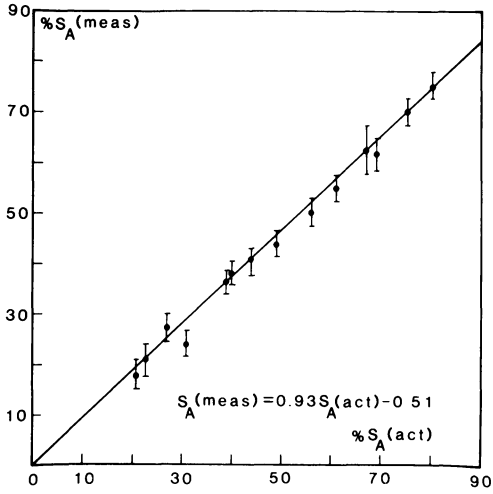

Figure 36. Measured versus actual percent area stenosis.

clinically significant. In any event, the measured values correlate quite well with the actual ones with a very small offset value. We thus conclude that the measurement of percent stenosis, i.e., relative volume of small objects, can be done videodensitometrically quite accurately without any corrections.

6.2. Absolute Volume Measurements

As we have seen before, the videodensitometric volume measurements are performed by integrating the gray levels within an ROI which encompasses the two-dimensional projection of the volume under consideration. Mathematically, the integration of gray levels within the ROI is expressed by

$$I = \int_{(x,y)} \int_{\epsilon \text{ ROI}} [\ln V_m(x,y) - \ln V_I(x,y)]dxdy \tag{62}$$

where V_m and V_I are the digital X-ray images before and after the introduction of the contrast agent into the volume of interest. We also point out that the mask image V_m is logarithmically subtracted pixel by pixel from the iodinated one V_I. The integrated signal I given in Eq. (62) actually is only proportional to the volume if the errors discussed in earlier sections are not serious. We can express this relationship as

$$I = k \cdot \text{volume} \tag{63}$$

where k is a constant of proportionality. Thus, absolute volume measurement using videodensitometric data (I) requires the determination of k. Kruger proposed a method[22] for the determination of k for small vessels by combining videodensitometric data with geometric assumptions about the object. A similar method was proposed by Henry and co-workers[23] which again utilized geometrical with videodensitometric information for the determination of ventricular volume. According to this method, it is assured that for the left ventricle, a region approximately two-fifths from the base has circular symmetry around the long axis of the ventricle. This is a less stringent assumption than the one which is used in the area–length method of left ventricular volume determination[24] where the ventricle is assumed to be an ellipsoid of revolution. If such a circular region exists, it may be used to determine k. This is done as follows. Let us assume that the circular region has a diameter D. If we pick a cylindrical slab of height H, then the geometrical volume of the slab is given by

$$V_0 = 0.25\pi HD^2 \tag{64}$$

We also need the videodensitometric signal from the same slab; let us call this I_0. According to Eq. (63), we have

$$I_0 = kV_0 \tag{65}$$

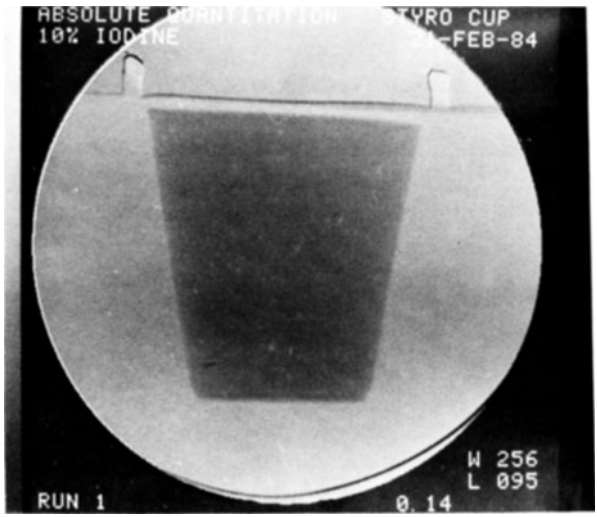

Figure 37. Subtracted Styrofoam cup filled with 10% Renografin-76 for absolute volume measurement.

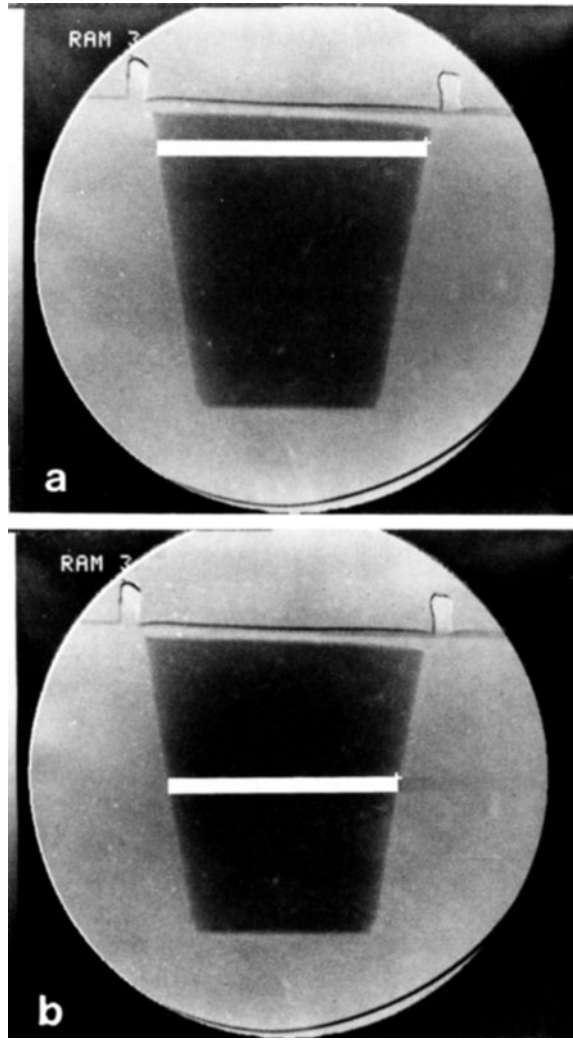

Figure 38. Selection of calibration ROIs: (a) top; (b) middle; (c) bottom.

which can be solved for k since we know both I_0 and V_0. By integrating the gray levels within the whole left ventricle, we obtain I_{LV} which is related to the ventricular volume by Eq. (63). Thus, we have

$$I_{LV} = kV_{LV} \tag{66}$$

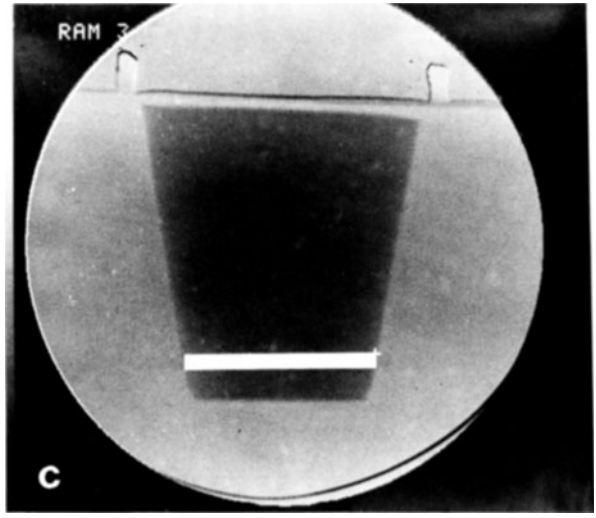

Figure 38. (*continued*)

Assuming that the contrast material is uniformly distributed within the ventricle, i.e., same constant in Eqs. (65) and (66), we can eliminate k and solve for V_{LV}. We obtain

$$V_{LV} = I_{LV}(V_0/I_0) \tag{67}$$

Equation (67) yields the absolute volume of the ventricle. An experimental simulation of this method was undertaken by filling a Styrofoam cup with water first (mask image) and then with a 10% solution of Renografin-76.[25] The exposure was made at 75 kVp with 4-mm aluminum filtration. The mask image was logarithmically subtracted from the iodinated one and the difference image is shown in Figure 37. Even though the cup is perfectly symmetric and all the dimensions are known, where to pick the calibration ROI still remains ambiguous. In order to test the influence of the location of calibration ROI on the final result, we used three different calibration ROIs. These were top, middle, and bottom of the cup as shown in Figure 38a–c. As a final check, we also mathematically simulated a cup of the same dimensions using the experimental projection data which were discussed in earlier sections. The actual volume of Renografin-76 solution within the cup was 150 cm^3. The results are given in Table 3. Experimentally determined absolute volumes vary from 168 to 140 cm^3 depending on the location of the calibration ROI, representing a change of error from

TABLE 3. Videodensitometric Absolute Volume Determination

Location of calibration ROI	Experimental		Computer simulation	
	Volume (cm^3)	% error	Volume (cm^3)	% error
Top	167.8	+11.9	166.7	+11.1
Middle	151.0	+0.7	149.0	−0.7
Bottom	140.0	−6.7	131.4	−12.4

+11.9 to −6.7%. For this object, the calibration ROI location in the middle yields the most accurate result. The results obtained by simulation using the experimental projection data reflect a similar behavior. The conclusion is that for an object which has a variable thickness, the location of the calibration ROI is important. Of course, if the data had not suffered from the degradation factors discussed earlier, the location of the calibration ROI would not have been important. This was tested by using the corrected projection data in the simulation. The calculated volumes were 150.9 and 151.1 cm^3 corresponding to the three calibration ROIs, indicating the insensitivity of the location of calibration ROI as expected. The conclusion drawn from this experiment is that even though one may obtain accurate absolute volume measurements for large objects, accuracy strongly depends on the location of the calibration ROI. In a real case with a patient, one never knows how much error is made if the images are not corrected prior to performing measurements. In the case of small objects, i.e., vessels, the errors would be much smaller even without any corrections, which is the same as before.

7. SUMMARY

In this chapter, we have discussed the various physical factors which cause the videodensitometric measurements performed with II–TV-based digital X-ray systems to be inaccurate. Experimental and simulation results demonstrating the contribution of each degradation factor were presented. We have shown that the degradation factors in increasing order of importance are beam hardening, veiling glare, and X-ray scatter within the patient. Various techniques for reducing the errors were introduced and discussed. In developing correction techniques, we avoided *empirical methods* such as background subtraction, lead disk placement on the object for scatter correction, and so on, since these methods work in limited situations and are not based on any sound physical principle. We

believe that empirical methods result in unpredictable results when the experimental conditions are altered.

It was shown that the correction methods presented here are quite accurate in reducing veiling glare and beam-hardening artifacts. A new technique was also introduced for scatter correction. An important observation was that the measurements of small volumes was affected less by degradation factors as compared to larger volumes, e.g., small vessels versus the heart. As pointed out, this difference is due to two regions of linearity, one for small and the other for large volumes. In the small volume region, the offset value of the straight line response curve was quite small, resulting in accurate volume measurements. For the case of large volumes, in spite of the straight line response, a large offset appears, causing all the videodensitometric measurements to be systematically underestimated. Claims made by various authors regarding the good linear correlation between the measured and actual EF values seem to ignore the systematic underestimation and instead focus only on linearity. Furthermore, when one attempts to confirm the accuracy of a method using patient data and other "gold standard" techniques, one can never be sure what the true value is. We believe that the accuracy of any method should be confirmed using realistic phantoms where many uncertainties are eliminated.

ACKNOWLEDGMENT. This work was supported in part by PHS Grants 1R01 CA35243-02 and 1R01 HL31440-01A1.

REFERENCES

1. N. A. Baily, Video techniques for x-ray imaging and data extraction from roentgenographic and fluoroscopic presentations, *Med. Phys.* **7,** 472–491 (1980).
2. B. G. Trenholm, D. A. Winter, D. Myrain, and E. L. Lansdown, *Med. Biol. Eng.* **10,** 163 (1972).
3. N. R. Silverman, Clinical videodensitometry, *Am. J. Roentgenol.* **114,** 814 (1972).
4. C. A. Mistretta, R. A. Kruger, T. L. Houk, S. J. Riederer, C. G. Shaw, D. Ergun, W. Kubal, A. B. Crummy, W. Ziebel, G. Rowe, W. Zarnstorff, and D. Flemming, Computerized fluoroscopy techniques for non-invasive cardiovascular imaging, *Proc. SPIE* **152,** 65–71 (1978).
5. C. A. Mistretta, in *The Physics of Medical Imaging: Recording System Measurements and Techniques* (A. G. Haus, ed.), Institute of Physics, New York (1979).
6. O. Nalcioglu, J. A. Seibert, W. W. Roeck, W. L. Henry, J. M. Tobis, and W. D. Johnston, Comparison of digital subtraction videodensitometry and area length method in the determination of left ventricular ejection fraction, *Proc. SPIE* **314,** 294–298 (1981).
7. R. A. Kruger, Time dependent subtraction imaging using computerized fluoroscopy, Ph.D. thesis, University of Wisconsin (1978).

8. M. Abramowitz and I. Stegun, *Handbook of Mathematical Functions,* Dover, New York (1964).
9. R. A. Kruger, C. A. Mistretta, and S. J. Riederer, Physical and technical aspects of computerized fluoroscopy difference imaging, *IEEE Trans. Nucl. Sci.* **28,** 205–215 (1981).
10. W. Hendee, *Medical Radiation Physics,* Year Book, Chicago (1970).
11. C. G. Shaw, D. L. Ergun, P. D. Myerowitz, M. S. Van Lysel, C. A. Mistretta, W. Zarnstorff, and A. B. Crummy, A technique of scatter and glare correction for video-densitometric studies in digital subtraction angiography, *Radiology* **142,** 209 (1982).
12. J. A. Seibert, O. Nalcioglu, and W. W. Roeck, A deconvolution technique for the improvement of contrast of image intensifiers, *Proc. SPIE* **314,** 310–318 (1981).
13. O. Nalcioglu, J. A. Seibert, J. M. Boone, Y. Wang, W. W. Roeck, W. L. Henry, J. M. Tobis, and W. D. Johnston, in *Digital Imaging in Cardiovascular Radiology* (P. H. Heintzen and R. Brennecke, eds.), Thieme, Stuttgart (1983).
14. J. A. Seibert, O. Nalcioglu, and W. W. Roeck, Removal of image intensifier veiling glare by mathematical deconvolution techniques, *Med. Phys.* **12,** 281 (1985).
15. J. A. Seibert, O. Nalcioglu, and W. W. Roeck, Characterization of the veiling glare PSF in x-ray image intensified fluoroscopy, *Med. Phys.* **11,** 172 (1984).
16. B. R. Frieden, in *Picture Processing and Digital Filtering* (T. S. Huang, ed.), Springer-Verlag, Berlin (1975).
17. E. O. Brigham, *The Fast Fourier Transform,* Prentice–Hall, Englewood Cliffs, N.J. (1974).
18. H. H. Barrett and W. Swindell, *Radiological Imaging,* Academic Press, New York (1981).
19. R. Bracewell, *The Fourier Transform and Its Applications,* McGraw–Hill, New York (1965).
20. E. C. McCullough, Photon attenuation in computer tomography, *Med. Phys.* **2,** 307 (1975).
21. J. G. Pearce, E. N. C. Milne, G. D. Gillan, and W. Roeck, Development of a radiographic chest phantom with disease simulation, *Invest. Radiol.* **14,** 181 (1979).
22. R. A. Kruger, Estimation of the diameter of and iodine concentration within blood vessels using digital radiography devices, *Med. Phys.* **8,** 652 (1981).
23. J. M. Tobis, Y. Wang, O. Nalcioglu, and W. Henry, Absolute left ventricular volume obtained by videodensitometry and DSA, *J. Am. Col. Cardiol.* **2,** 616 (1983).
24. H. T. Dodge, H. Sandler, D. Ballew, and J. D. Lord, The use of biplane angiocardiography for measurement of left ventricular volume in man, *Am. Heart J.* **60,** 762 (1960).
25. J. A. Seibert, O. Nalcioglu, J. Tobis, W. Roeck, and W. Henry, Factors influencing quantitation of absolute ventricular volume by digital subtraction angiography, in press.